IJCOE
COASTAL, OFFSHORE & ENVIRONMENTAL ENGINEERING

Volume 1 | Issue 2 | Jul 2016

www.ijcoe.org info@ijcoe.org

International Journal of Coastal, Offshore and Environmental Engineering (IJCOE)
Vol. 1 / Issue 2 / Jul 2016
2

Since 2015
International Journal of Coastal, Offshore & Environmental Engineering

Volume 1 | Issue 2 | Jul 2016

IJCOE
Editor-in-Chief: Prof. Hamid S.Bahai

International Journal of Coastal, Offshore & Environmental Engineering
Since 2015
ISSN: 2980-8721 (online)

In The Name of God

Message from the Editor-in-Chief

The IJCOE journal office was established in 2015,and its first issue was published in 2016. TheIJCOE covers a wide range of research in thefields of oceanography & ocean technology, aswell as marine industries & marine engineering.The editorial board of IJCOE consists of nearly130 of the greatest scientists and researchersfrom over 30 countries worldwide, and thejournal's review board comprises 1,000 membersfrom all five continents. The membership andapplication process for joining the editorial andreview boards of this journal is ongoing. IJCOE isa research-academic quarterly journal that haspublication and distribution permissions fromthe Press Organization and permission topublish scientific-research articles from theMinistry of Science, Research, and Technology(MSRT) with an "A" rating. It also holds a "Q1"rating from the ISC institute with an impactfactor (IF) of approximately 0.43 and isconsidered a "core journal" (prestigious andoutstanding journal). IJCOE is an open-accessjournal and allows the download and receipt ofaccepted articles in full text for free. It respectsand adheres to copyright and COPE regulations.The journal's office operates 24/7, providingservices to researchers. In addition to publishinga regular quarterly journal, IJCOE has 16 specialissues on specific topics in preparation. It alsoprovides conditions for publishing specializedbooks, references, and handbooks. Moreover, itis ready to cooperate with the secretariats ofreputable international conferences to publishtheir selected and outstanding articles. IJCOEevaluates, appraises, and publishes books,articles, and the scientific achievements andfindings of esteemed researchers and scientistsworldwide who are innovating and conductingin-depth research in the "important and strategicfield of the maritime technology & Oceanengineering." It welcomes any form of jointcooperation with universities, research institutes,and related research centers at the national,regional, and international levels, and extends ahand for collaboration.

Classification of Editorial Board in IJCOE

Editor-in-Chief

Director-in-Chief

Deputy Editor

Executive Managers

English Text Editor

Technical Editor

International Editorial Board

National Editorial Board

Editorial Board Associate

Editorial Board Assistant

Guest Editorial Board

Advisory Board

Administrative Coordinator

Honorary Board Member

Methodology Advisor

Author Benefits

- Open Access
- Rapid Publication
- Thorough Peer-Review
- No Copyright Constraints
- Coverage by Leading Indexing Services
- Discounts On Article Processing Charges (APC)
- No Space Constraints, No restriction on the maximum length of the papers, number of figures or colors

INTERNATIONAL JOURNAL OF IJCOE COASTAL, OFFSHORE & ENVIRONMENTAL ENGINEERING

Aims of IJCOE

Hydrodynamics

Marine equipment

Structural mechanics

Ocean environmental predictions

Stochastic calculations Experimental

Automatic Control of Marine Systems

Scope of IJCOE

Marine Hazards

Ocean Acoustics

Naval Architecture

Ocean Engineering

Coastal Engineering

Marine Meteorology

Marine Earth Sciences

Underwater Technology

Marine Renewable Energy

Polar & Arctic Engineering

Marine Renewable Energy

Marine Geography & Geodesy

Marine Environmental Engineering

Automatic Control of Marine Systems

Hydro Physics & Physical Oceanography

Type of papers

- Case Studies
- Book Reviews
- Review Article
- Letters to the Editor
- Methodology Papers
- Editorials and Commentaries
- Response or Rejoinder Papers
- Perspective or Opinion Papers
- Conceptual or Theoretical Papers
- Meta-Analysis and Systematic Reviews
- Short Communications or Brief Reports
- Research Articles (Original Research Papers)

Scientific Research Journal

Ministry of Science, Research And Technology (MSRT)

Jurnal Ranking 2023: A

Ministry Of Science, Research And Technology (ISC)

Citation Impact 2022: 0.429

Quartile 2022 : Q1

Core Collection

IJCOE is a Member of

Cantact Us

Office 1 | Research Institute of Meteorology and Atmospheric Science

Address | Tehran, Shahid Kharrazi Highway, Pajoohesh Blvd, Research Institute of Meteorology and Atmospheric Science, Sand and Dust Storm International Research Center (SDS-IRC), No. 13, 1st floor.

Phone | +982144787652

Postal code | 13611-14977

website | www.rimac.ac.ir

Office 2 | Iranian National Institute for Oceanography and Atmospheric Science

Address | Tehran, Dr. Fatemi Gharbi St., Shahid Etemadzade St., No. 3, third floor.

Phone | +982166944873

Postal code | 13389 – 14118

website | www.inio.ac.ir

Email | Info@ijcoe.org

Website | www.ijcoe.org

Follow Us

www.ijcoe.org

INTERNATIONAL JOURNAL OF IJCOE COASTAL, OFFSHORE & ENVIRONMENTAL ENGINEERING

Volume & Issue:

Volume 1, Issue 2, July 2016

Number of Articles: 5

Content

INTERNATIONAL JOURNAL OF
COASTAL & OFFSHORE ENGINEERING IJCOE No. 2/Spring 2016 (1-7)

Design of Control Strategy for Swarm Autonomous Vessels for Circling Mission in Calm Water

Hassan Sayyaadi[1]*, Abbas Ghasemzade Ahrami[2]

[1] *Associated Professor, Center of Excellence in Hydrodynamics and Dynamics of Marine Vehicles, School of Mechanical Engineering, Sharif University of Technology; sayyaadi@sharif.edu*
[2] *Master student, School of Mechanical Engineering, Sharif University of Technology; abbas-gh68@hotmail.com*

ARTICLE INFO

Article History:
Received: 23 Mar. 2016
Accepted: 15 Jun. 2016

Keywords:
Multi-agent system, Group coordination, nonlinear control, Swarm; Surface vessel, Autonomous vessel, Formation control, Vessel dynamics

ABSTRACT

Control of a group of autonomous surface vessels, called agents, with realistic dynamic for circling mission is addressed with the aid of Lyaponov and graph theory. In this brief, to obtain a cooperative controller in between agents, new coordination transfer are presented and graph theory is used to illustrate communication between the agents. With the aid of Lyaponov theory and graph theory application, decentralized and scalable controllers are designed for group of autonomous vessels to converge to a desired geometry for circling around a specific target point. Due to the realistic agent dynamics, non-holonmic dynamics and turning constrains of the vessels are considered in the design process. Advantage of the proposed controller is: it uses domestic information between agents and the controller is designed based on these information. The agents herein represent a large class of autonomous vessels with realistic limitation on vessel motion. Besides, in previous works inertia and damping matrix of the agents were assumed to be diagonal and constant, in this research work non-diagonal inertia matrix and variable damping matrix are under consideration. MATLAB and Simulink are used to represent the effectiveness of the proposed controllers. As the simulation results show, designed controllers perform well on the system and the objective duty is achieved appropriately.

1. Introduction

As autonomy and unmanned systems grow, autonomous vessels have fascinated and attracted the interest of researchers for many years. These systems are recognized as unmanned vessels for many potential and defence application including search and rescue operations, surveillance and others.

A multi agent system is computerized system composed of multiple interacting agents within an environment. Multi agent systems can be used to solve problems that are difficult or impossible for an individual agent or monolithic systems to solve. Most of the researches are focused on studies on the dynamic and control of multi agent systems. Therefore, design of control strategy for this kind of systems is interested in recent decade. A great deal effort has been directed at developing centralized and decentralized control strategy for wide variety of swarm application. In [1] artificial potential and virtual leaders are used for swarm control. Null space based behavioral control are explained in [2] for formation control of under actuated surface vessels. In [3] back stepping method are addressed and in [4] authors use sliding mode tracking control for surface vessels. Authors in [5] used modified bees algorithm, and in [6] used distance estimation schemes, and in [7] local adaptive internal model based controllers are presented. In this paper, Lyaponov and graph theory are used for design of control strategy for swarm formation of multiple vessels in calm water. This method is based on [8], but cannot be used directly because the model which is selected here, is a real and has more complicated dynamics influences. In other hand, the controller designed in [8] is used for small surface vessels but the model used in this paper is the real tug boat, has a total length of 30 meters.

The remaining of the paper is organized as; in section 2 dynamic model of the tug boat is derived and then coordination transfer is proposed. Mission statement is addressed in section 3 and then cooperative controllers are proposed in section 4. Finally, simulation results are depicted in section 5.

2. Model Dynamic

Consider the *N* actuated three DOF planar vessels which is illustrated in figure 1. Surge propulsive force is delivered by a propeller and a rudder provide torque capable of affecting yaw. Dynamics model of each vessel can be given in equation 1 to equation 7 appropriately [9] and dynamics equations for the *i*'th vessels can be written as:

$$\eta_i = \begin{bmatrix} x_i \\ y_i \\ \theta_i \end{bmatrix} \; and \; v_i = \begin{bmatrix} u_i \\ v_i \\ r_i \end{bmatrix} \tag{1}$$

$$\dot{\eta}_i = R(\theta_i) v_i \tag{2}$$

$$R(\theta_i) = \begin{bmatrix} \cos(\theta_i) & -\sin(\theta_i) & 0 \\ \sin(\theta_i) & \cos(\theta_i) & 0 \\ 0 & 0 & 1 \end{bmatrix} \tag{3}$$

$$M_i \dot{v}_i + \big(C_i + D_i(v_i)\big) v_i = \begin{bmatrix} \tau_1 \\ 0 \\ \tau_3 \end{bmatrix} \tag{4}$$

$$M_i = \begin{bmatrix} m_{i11} & 0 & 0 \\ 0 & m_{i22} & m_{i23} \\ 0 & m_{i32} & m_{i33} \end{bmatrix} \tag{5}$$

$$D_i = \begin{bmatrix} d_{i11} + d_{i11}^n |u_i| & 0 & 0 \\ 0 & d_{i22} & d_{i23} \\ 0 & d_{i32} & d_{i33} \end{bmatrix} \tag{6}$$

Where:

- (x_i, y_i) is the location of mass center
- L_i is the total vessel length
- L_{cgi} is the distance from the mass center to the vessel bow
- u_i is the surge speed of the vessel in its body frame
- v_i is the sway speed in the body frame
- θ_i is the yaw angel in the world coordinate frame
- τ_1 is the thrust generated by the prime mover
- τ_3 is the yaw torque generated by the rudder system
- M_i is the inertial matrix for vessel *i*
- D_i is the damping matrix for vessel *i*
- C_i is the term representing the Coriolis and centrifugal forces.

The control inputs for this under actuated system are τ_1 and τ_3 which have to control three state variables of the system through a nonlinear equations. These equations also consist nonholonomic constraints which bring limitation on velocities to be performed. Every vessel will be operating in displacement mode, so the weight of vessel is supported by buoyant force.

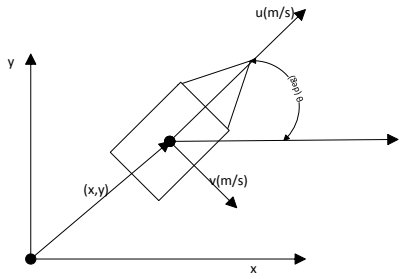

Fig. 1. Autonomous surface vessel model

3. Mission Statement

Considering *N* under actuated surface vessels. During control mission, each vessel knows its own state and the states of some neighboring vessels by communication links [8]. This communication topologies will be described by the aid of graph theory. It is assumed that all agents know its owns states and the states of some other vessels.
Given a desired geometric pattern P defined by constant vectors $[p_{jx}, p_{jy}]$ for$1 \le j \le n$, assuming:

$$\sum_{j=1}^{n} p_{jx} = 0, \quad \sum_{j=1}^{n} p_{jy} = 0 \tag{8}$$

Based on the desired trajectory, designing a cooperative controller for each vessel such that [8]:

$$\lim_{t\to\infty} \left(\begin{bmatrix} x_i - x_j \\ y_i - y_j \end{bmatrix} - \begin{bmatrix} p_{ix} - p_{jx} \\ p_{iy} - p_{jy} \end{bmatrix} \right) = \begin{bmatrix} 0 \\ 0 \end{bmatrix} \tag{9}$$

$$\lim_{t\to\infty} \big(\theta_j - \theta_d\big) = 0 \tag{10}$$

$$\lim_{t\to\infty} \big(u_j - u_d\big) = 0 \tag{11}$$

$$\lim_{t\to\infty} \big(v_j - v_d\big) = 0 \tag{12}$$

$$\lim_{t\to\infty} \big(\dot{\theta}_i - \dot{\theta}_d\big) = 0 \tag{13}$$

To achieve these control targets, coordination transfer is proposed here. Following the work [8], the new errors are defined base on system dynamics. The new errors are defined as:

$$\lim_{t\to\infty} e_j = \lim_{t\to\infty} \left(\begin{bmatrix} x_j \\ y_j \\ \theta_j \\ u_j \\ v_j \\ \dot{\theta}_j \end{bmatrix} - \begin{bmatrix} x_d + p_{jx} \\ y_d + p_{jy} \\ \theta_d \\ u_d \\ v_d \\ \dot{\theta}_d \end{bmatrix} \right) = 0 \tag{14}$$

So the cooperative controller in between agents

should be design in such a way that the above control scheme to be achieved. Based on the agents' dynamic, new tracking errors are defined and the controller will be tuned based on these new errors. Tracking errors are defined as:

$$\begin{aligned}\delta_{1j} = {} & (x_j - p_{jx})\cos(\theta_j) \\ & + (y_j - p_{jy})\sin(\theta_j) \\ & - (x_d\cos(\theta_d) \\ & + y_d\sin(\theta_d)\end{aligned} \tag{15}$$

$$\delta_{2j} = v_j - v_d \tag{16}$$

$$\begin{aligned}\delta_{3j} = {} & -(x_j - p_{jx})\sin(\theta_j) \\ & + (y_j - p_{jy})\cos(\theta_j) \\ & + \frac{m_2}{d_2}v_j - (-x_d\sin(\theta_d) \\ & + y_d\cos(\theta_d) + \frac{m_2}{d_2}v_d)\end{aligned} \tag{17}$$

$$\delta_{4j} = \theta_j - \theta_d \tag{18}$$

$$\delta_{5j} = \dot{\theta}_j - \dot{\theta}_d + k_4\delta_{4j} \tag{19}$$

$$\delta_{6j} = -\frac{m_1}{d_2}u_j - \delta_{1j} + \frac{m_1}{d_2}u_d + k_3\delta_{5d}\delta_{3j} \tag{20}$$

These new inputs coordinates are different from those three in planar maneuver of any vessel [8]. These transfer coordinates are defined as:

$$\begin{aligned}w_{1j} = {} & \left(\frac{d_1}{d_2} - 1\right)u_j - \delta_{3j}\delta_{6j} - \frac{\tau_{1j}}{d_2} \\ & - (-m_{32}\dot{v}_d - \frac{d_{32} + c_{32}}{m_{32}}v_d \\ & - \frac{c_{33}}{m_{33}}\dot{\theta}_d + \frac{\tau_{2d}}{m_{33}})\end{aligned} \tag{21}$$

$$\begin{aligned}w_{2j} = {} & -m_{32}\dot{v}_j - \frac{d_{32} + c_{32}}{m_{32}}v_j - \frac{c_{33}}{m_{33}}\dot{\theta}_j \\ & + \frac{\tau_{2j}}{m_{33}} - (\left(\frac{d_1}{d_2} - 1\right)u_d \\ & - \delta_{3d}\delta_{5d} - \frac{\tau_{1d}}{d_2})\end{aligned} \tag{22}$$

The new errors are defined as $\delta_* = [\delta_{1j}, \delta_{2j}, \delta_{3j}, \delta_{4j}, \delta_{5j}, \delta_{6j}]$. It is easy to show that if $\lim_{t\to\infty}\delta_* = 0$, then $\lim_{t\to\infty} e = 0$ achived. The dynamics of tracking errors are:

$$\begin{aligned}\dot{\delta}_{1j} = {} & -\frac{d_2}{m_1}\delta_{1j} - \frac{d_2}{m_1}(\delta_{6j} - k_3\delta_{5j}\delta_{3j}) \\ & + \delta_{3j}(\delta_{5j} - k_4\delta_{4j}) \\ & + \delta_{3d}(\delta_{5j} - k_4\delta_{4j}) \\ & + \delta_{5d}\delta_{3j} \\ & - \frac{m_2}{d_2}[\delta_{2j}(\delta_{5j} - k_4\delta_{4j}) \\ & + \delta_{2d}(\delta_{5j} - k_4\delta_{4j}) \\ & + \delta_{2j}\delta_{5d}]\end{aligned} \tag{23}$$

$$\begin{aligned}\dot{\delta}_{2j} = {} & -\frac{d_2}{m_2}\delta_{2j} + \frac{d_2}{m_2}[\delta_{1j}(\delta_{5j} - k_4\delta_{4j}) \\ & + \delta_{1d}(\delta_{5j} - k_4\delta_{4j}) \\ & + \delta_{1j}\delta_{5d} \\ & + (\delta_{5j} - k_4\delta_{4j})(\delta_{6j} \\ & - k_3\delta_{5d}\delta_{3j}) \\ & + (\delta_{5j} - k_4\delta_{4j})\delta_{6d} \\ & + \delta_{5d}(\delta_{6j} - k_3\delta_{5d}\delta_{3j})]\end{aligned} \tag{24}$$

$$\begin{aligned}\dot{\delta}_{3j} = {} & (\delta_{5j} - k_4\delta_{4j})(\delta_{6j} - k_3\delta_{5d}\delta_{3j}) \\ & + (\delta_{5j} - k_4\delta_{4j})\delta_{6d} \\ & + \delta_{5d}(\delta_{6j} - k_3\delta_{5d}\delta_{3j})\end{aligned} \tag{25}$$

$$\dot{\delta}_{4j} = -k_4\delta_{4j} + \delta_{5j} \tag{26}$$

$$\dot{\delta}_{5j} = w_{1j} - w_{1d} + k_4(-k_4\delta_{4j} + \delta_{5j}) \tag{27}$$

$$\begin{aligned}\dot{\delta}_{6j} = {} & w_{2j} - w_{2d} + k_3\dot{\delta}_{5d}\delta_{3j} \\ & + k_3\delta_{5d}(\delta_{5j} - k_4\delta_{4j})(\delta_{6j} \\ & - k_3\delta_{5d}\delta_{3j}) \\ & + k_3\delta_{5d}(\delta_{5j} - k_4\delta_{4j})\delta_{6d} \\ & + k_3\delta_{5d}^2(\delta_{6j} - k_3\delta_{5d}\delta_{3j})\end{aligned} \tag{28}$$

Based on the [8], following lemmas are addressed:
Lemma 1: For the variables defined in the above formulas, if:

$$\begin{aligned}\lim_{t\to\infty}(\delta_{ij} - c_i) = 0 \quad & (1 \le i \le 6,\ 1 \le j \\ & \le m)\end{aligned} \tag{29}$$

Where c_i are bounded variables, then equation 9 is being satisfied. Furthermore, if $c_i = 0$ for$(1 \le i \le 6)$, then equations 9 to 13 are being satisfied.
Lemma 2: For system equations 15 to 20, if $\delta_{5j}\ and\ \delta_{6j}$ exponentially converge to constants $c_5\ and\ c_6$, respectively, for $1 \le j \le m$, then equation 9 is being satisfied. Furthermore, if $c_5 = c_6 = 0$, then equations 9 to 13 are being satisfied, which means that the cooperative control problem is achieved.

4. Communication Digraph

Assumption 1: The communication digraph *G* is fixed and has a spanning tree.
Given any $m * m$ constant matrix $A = [a_{ji}]$ with $a_{ji} > 0$ for $1 \le i, j \le m$, the Laplacian matrix $L = [L_{ji}]$of

the digraph G with weight matrix A is defined as:

$$L_{ji} = \begin{cases} -a_{ji} & if\ i \neq j\ and\ i \in N_j \\ 0 & if\ i \neq j\ and\ i \in N_j \\ \sum_{l \neq j, l \in N_j} a_{jl} & if\ i = j \end{cases} \quad (30)$$

Lemma 3: L is the Laplacian matrix of the digraph G with weight matrix $A = [a_{ji}]$ and $a_{ji} > 0$. If the digraph G satisfies Assumption 1, then:

$$\lim_{t\to\infty} e^{\mu t}\left(e^{-Lt} - 1w_l^T\right) = 0 \lim_{t\to\infty} e^{\mu t}\left(e^{-Lt} - 1w_l^T\right) = 0 \quad (31)$$

For any $\mu \in \left[0, Re\left(\lambda_2(L)\right)\right]$, where w_l satisfies $w_l^T L = 0$ and $w_l^T 1 = 1$. Accordingly [10].

5. Cooperative Control laws

For the systems in equations 1 to 7, regarding to Lemma 1, 2 and 3 and assumption 1, control laws are:

$$\begin{aligned} \tau_{1j} = \sum_i & d_2 a_{ji}\left(\delta_{5j} - \delta_{5i}\right) - d_2 w_{1d} \\ & + d_2 k_4\left(-k_4\delta_{4j} + \delta_{5j}\right) \\ & + (d_1 - d_2)u_j - d_2\delta_{3j}\delta_{6j} \\ & - d_2(-m_{32}\dot{v}_d \\ & - \frac{d_{32} + c_{32}}{m_{32}} v_d - \frac{c_{33}}{m_{33}}\dot{\theta}_d \\ & + \frac{\tau_{2d}}{m_{33}}) \end{aligned} \quad (32)$$

$$\begin{aligned} \tau_{2j} = -\sum_i & m_3 a_{ji}\left(\delta_{6j} - \delta_{6i}\right) + m_3 w_{2d} \\ & - m_3 k_3 \dot{\delta}_{5d}\delta_{3j} \\ & - m_3 k_3 \delta_{5d}\left(\delta_{5j}\right. \\ & \left. - k_4\delta_{4j}\right)\left(\delta_{6j} - k_3\delta_{5d}\delta_{3j}\right) \\ & - m_3\, k_3\delta_{5d}\left(\delta_{5j}\right. \\ & \left. - k_4\delta_{4j}\right)\delta_{6d} \\ & - m_3 k_3 \delta^2{}_{5d}\left(\delta_{6j}\right. \\ & \left. - k_3\delta_{5d}\delta_{3j}\right) \\ & - (m_1 - m_2)u_j v_j + d_3\dot{\theta}_j \\ & + m_3\left(\left(\frac{d_1}{d_2} - 1\right)u_d\right. \\ & \left. - \delta_{3d}\delta_{5d} - \frac{\tau_{1d}}{d_2}\right) \end{aligned} \quad (33)$$

Which $a_{ji} > 0, k_3 > 0, and\ k_4 > 0$.

Group of surface vessels approach to the desired pattern by the control laws in equation 32 and equation 33. Besides, these control laws have decentralized and scalable properties while performing proceed. Simulation results in [8] are used for small crafts and vessels with very simple dynamics, while proposed approach here have more generality.

6. Simulation results

The performance of the control laws are shown in following figures, tables, and discussions. In this research work, 3 surface tug boats which basic dynamic parameters were adopted from [9], are under control to converge to a desired pattern in distance from the target. Assume that the communication digraph is fixed. Control parameters are as: $a_{ij} = 1, k_3 = 20\ and\ k_4 = 20$. Initial conditions corresponding to the vessels are given in table I.

TABLE I. . INITIAL CONDITION OF 3 SURFACE VESSELS

$[x_1(0), x_2(0), x_3(0)]$	[25,25,25][m]
$[y_1(0), y_2(0), y_3(0)]$	[20,30,25][m]
$[\theta_1(0), \theta_2(0), \theta_3(0)]$	$\left[\frac{\pi}{4}, \frac{\pi}{6}, 0\right]$[rad]
$[u_1(0), u_2(0), u_3(0)]$	[0,0,0][m/s]
$[v_1(0), v_2(0), v_3(0)]$	[0,0,0][m/s]
$[r_1(0), r_2(0), r_3(0)]$	[0,0,0][rad/s]

Figure 2 demonstrates the entire formation trajectories of the systems. Figure 3 and 4 show that the control efforts with surge force and steering torque are bounded. Consequently, figures 3 and 4 confirms that the level of control activity is reasonable, and no saturation has occurred during the process. Figure 5 show that the velocities of the every agents during the circling mission are in reasonable margins and do not exceed to infinite values. Figures 6 shows excellent error convergences after an initial transient error associated with the nonholonomic nature of the unit agents. Figure 7 and 8 show the trajectory path of the fore and seven agents. They demonstrate the scalability of the system.

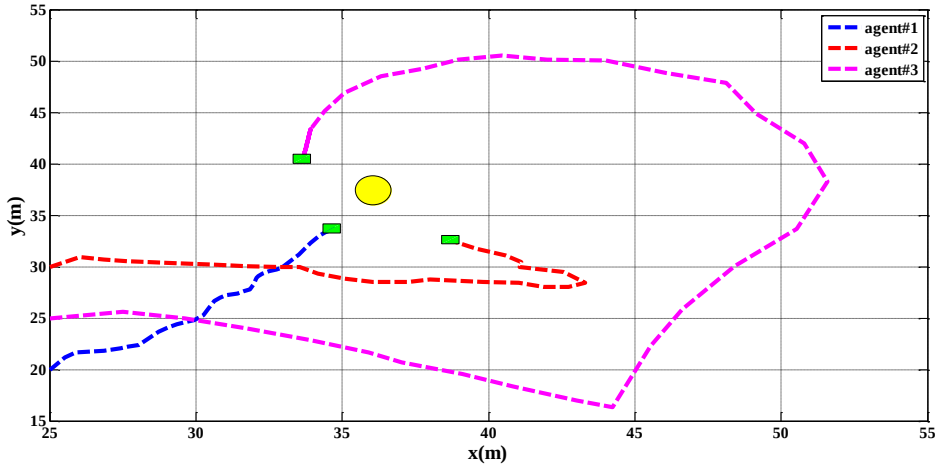

Fig. 2. Formation trajectory of the system circling around target.

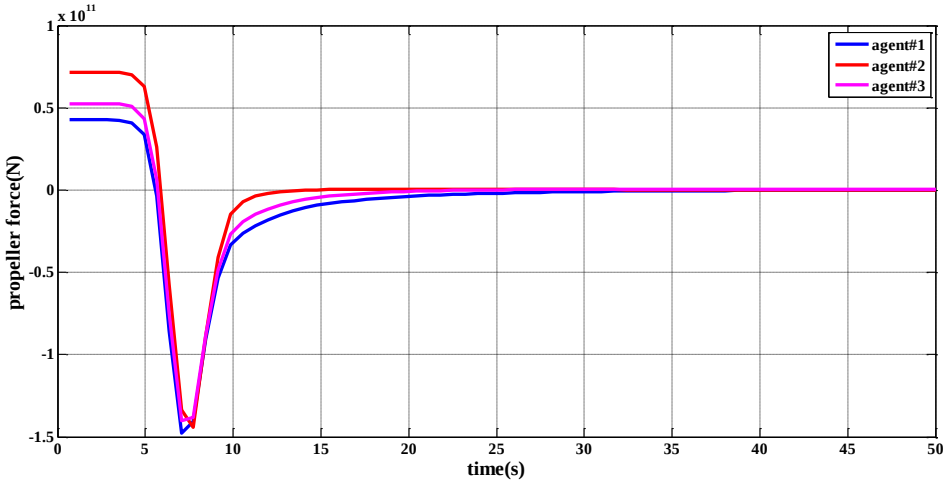

Fig. 3. Surge force time history.

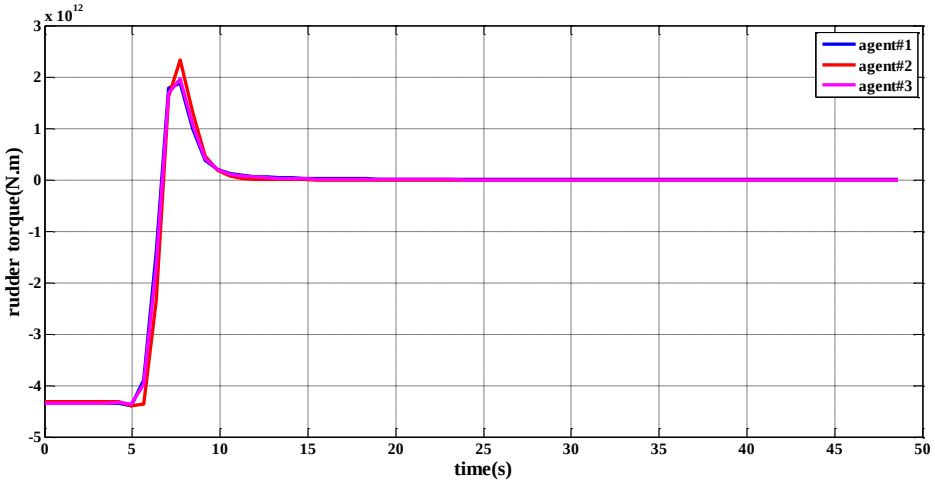

Fig. 4. . Steering torque time history.

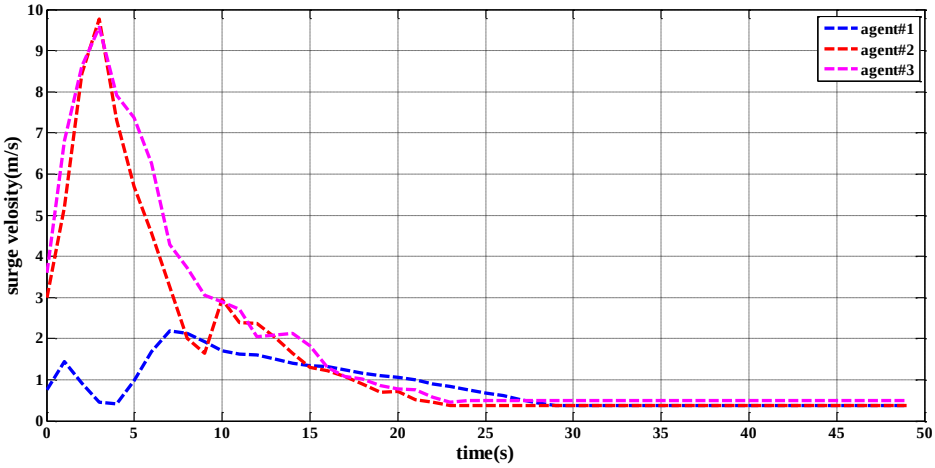

Fig. 5. Surge velocity .

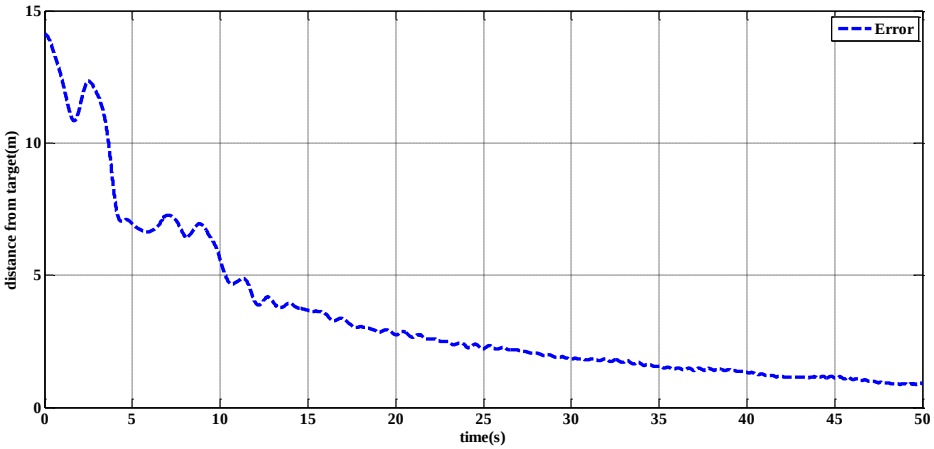

Fig. 6. The distance of the swarm center from target position

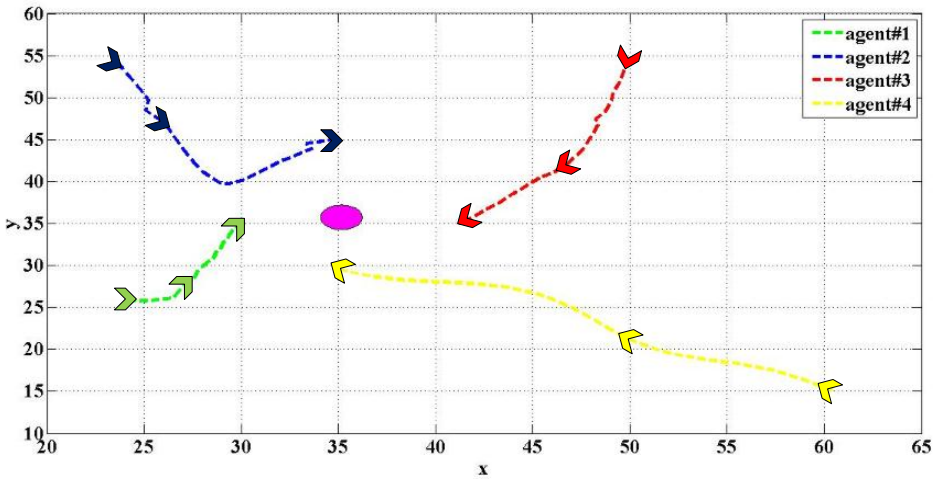

Fig. 7. Trajectory and coordinated control of four agents

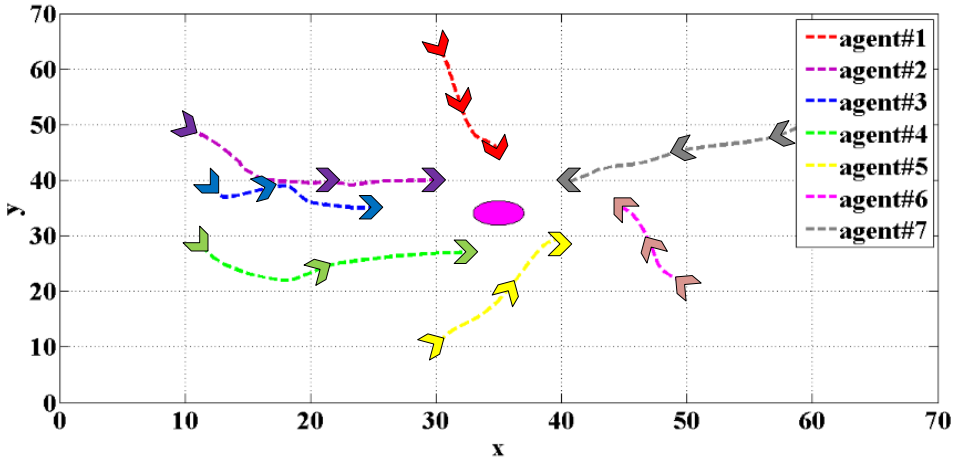

Fig. 8. Trajectory and coordinated control of seven agents

7. Conclusion

In this paper, a decentralized and scalable cooperative controller is proposed for a group of surface vessels with Non-Holonomic dynamic to converge to desired pattern in calm water. The controller laws are based on Lyaponov and Graph theorems, using suitable coordinate transformation. As the simulation results show, effectiveness of the proposed controller laws is achieved. Due to high order of Hydrodynamic matrix elements of the agents, level of control activities are reasonable and no saturation occurs during the mission.

REFERENCES

[1] Naomi, E.L., Edward, F., (2001), *Virtual Leaders, Artificial Potentials and Coordinated Control of Groups*, Proceeding of the 40th IEEE Conference on Decision and Control, Orlando, Florida USA, Vol.3, p.2968-2973.

[2] Filippo, A., Stefano, C., Thor, I.F., (2006), *Formation Control of Under actuated Surface Vessels using the Null-Space-Based Behavioral Control*, Proceeding of the IEEE/RSJ, International Conference on Intelligent Robotic and System, Beijing, China, p.5942-5947.

[3] Travis, D., Jagannathan, S.,(2007), *Control of Nonholonomic Mobile Robot Formations: Back stepping Kinematics into Dynamics*, 16th IEEE International Conference on Control Applications, Singapore, p.94-99.

[4] Hashem, A., Kenneth, R.M.,Lucas, C.M., reza, A.S., *Sliding-Mode Tracking Control of Surface Vessels*,(2008), IEEE Transactions on industrial Electronics, Vol.55, p.4004-4012.

[5] Jevtic, A., Gazi, P., Andina, D.,Jamshidi, M.,(2010).,*Building a swarm of robotic bees*, World Automation Congress(WAC), p.1-6.

[6] Fidan, B., Gazi, V., Shaohao, Z., Na, C., Karatas, E.,(2013)., *Single view Distance estimation Based Formation Control of Robotic Swarms*, industrial electronics, IEEE., Vol.60, P.5781-5791.

[7] Gazi, V., (2014)., Distributed output agreement in class of uncertain linear heterogeneous multi agent dynamic systems, European Control Conference(ECC), p.177-183.

[8] Dong, W.,(2010)., cooperative Control of under actuated surface vessels,IET Control Theory And Applications, Vol.4., p.1569-1580.

[9] Bradley, E.B., (2012)., *Formation Control of Under Actuated Autonomous Surface vessels using Redundant manipulator Analogs*, IEEE International Conference on robotic and Automation(ICRA)., p.4892-4897.

[10] Ihle, I.A., Jouffroy, J., Fossen, T.I.,(2006)., *Robust Formation Control of marine craft using lagrange multipliers*, Springer-Verlag.

[11] kristin, Y.P., Jan,T.G., Henk, N.,(2006)., *Group Coordination and Cooperative Control*, Springer-Verlag

[12] Veysel, G., Kevin, M.P., (2011)., *Swarm Stability and optimization*, Springer-Verlag.

[13] Chung, F.R.K.,(1997)., *Spectral graph theory*, Regional Conf.Series in Mathematics of Amer, Mathematical Soc, Vol.92.

[14] Merris, R.,(1998)., *Laplacian Graph eigenvectors*, Linear algebra Appl., p.221-236.

[15] Dong, W., Farrell, J.A.,(2008*), formation control of multiple underactuated surface vessels*,IET Control Theory and Applications, Vol.2, p.1077-1085.

[16] Lucas, C.M., Hashem,A., (2011), *Predictive and Sliding mode Cascade Control for Unmanned Surface Vessels*, American Control Conference(ACC), p.184-189.

INTERNATIONAL JOURNAL OF
COASTAL & OFFSHORE ENGINEERING
IJCOE No. 2/Spring 2016 (9-16)

Using Refined Simplified Model for Damage Detection in Offshore Jacket Structures

Farhad Hosseinlou[1], Alireza Mojtahedi[2], Mohammad Ali Lotfollahi Yaghin[3]

[1]*PHD candidate, Civil Engineering Department, University of Tabriz; F.Hosseinlou@tabrizu.ac.ir*
[2]*Associate professor, Civil Engineering Department, University of Tabriz; Mojtahedi@tabrizu.ac.ir*
[3]*Professor, Civil Engineering Department, University of Tabriz; Lotfollahi@tabrizu.ac.ir*

ARTICLE INFO

Article History:
Received: 20 Apr. 2016
Accepted: 15 Jun. 2016

Keywords:
simplified platform model, damage detection, model updating

ABSTRACT

This work introduces a structural integrity assessment strategy for Jacket structures based on the finite element model updating and a novel simplified method. Hereof, model reducing and model updating procedure is established based on a optimization technique. Since the number of measured degrees of freedom is most of the time restricted in practice, this paper represents a methodology using the cross model cross mode method (CMCM) in combination with an iterative procedure which uses limited, spatially incomplete modal information. This research is an empirical study on a laboratory model of a jacket structure with the aim of establishing Refined Simplified FE Model (RSM) to conduct damage detection. In addition to elimination of uncertainty effects in the damage detection results, RSM technique is employed because of practical considerations and also this technique provides a fast damage zone diagnosis procedure. Also, improved reduction scheme is utilized based on static reduction scheme to carry out damage detection in jacket structure.

1. Introduction

Integrity monitoring of the marine structures is very important and undeniable. For more marine structures, numerous studies have been presented in damage identification field, such as [1-6]. Structural damage induces alterations in physical properties and modal characteristics of the jacket structure. These changes have long been applied to detect damage. Also, structural model updating is often utilized for structural integrity assessment (SIA): by calibrating stiffness parameters of FE models based on experimentally obtained information, structural damage can be determined [7]. In the damage diagnosis process, numerical models are employed to simulate the behavior of real structure. But errors from the numerical model and the modeler are inevitable, which reflect in the difference between the FE model and the experimental model. The uncertainty in the results between the numerical modal analysis and the experimental modal analysis is because of the assumptions made in defining numerous unknown or uncertain system properties [8, 9]. Accordingly, the validity of the adopted numerical models is necessary. Structural model updating improves a numerical FE model utilizing experimental modal data to produce a refined model that better predicts the dynamic behavior of a real structure. Among the damage diagnosis algorithm, the techniques based on the modal parameter identification along with vibration testing and model updating process have received increasing attentions of researchers [10-12]. As evidenced in the literature, because of the many practical challenges encountered in such techniques, efforts at further improving these techniques for marine structures were largely abandoned by the early 1980s [13]. In this regard, during recent years a few researchers have discussed about the SIA in fixed marine structures. But, despite of the aforementioned effort, there is not any research which directly focused on the effects of the mentioned challenges as the main objective of the study to circumvent these major problems along utilizing the concept of mentioned approaches for jacket structures. To summarize, the improvement of SIA methodologies for offshore jacket platforms is aiming to provide safety, cost saving (maintenance) as well as environmental benefits. But, the number of successful practical applications of Structural Integrity Monitoring (SIM) technologies is still limited. This research introduces a new technique to evaluate SIM system for offshore jacket platform and apply it to an experimental case study (SPD9 platform jacket

located of the Persian Gulf). In this study, reduction process includes the decrease of the members of the structural model (simplified platform model) and the reduction of degrees of freedoms (static reduction). In this regard, an optimization-based model reducing approach is presented to reduce the members of the structural model by preserving the properties of the structure dynamic behavior. Hence, the first target of the current study is to carry out FE model updating based on modal-domain method utilizing frequency response technique (FRT). The FRT directly utilizes the measured frequency response functions (FRFs) for FE model updating. Since the FRT has numerous advantages over the other updating methods, the work concentrates on this technique. An improved reduction technique (static reduction) associating the model updating process is also utilized. Improved reduction technique removes the bad effect of model reduction process on the proposed method. Moreover, this technique prevents the appearance of spurious modes in the frequency range of interest. It is worth mentioning, the considered technique of the both optimization-based model reducing and model updating process is established utilizing a Computational Intelligence (CI) method. This technique is called Refined Simplified Model (RSM) technique. In other words, we introduced the novel simplified method (RSM) in both model reducing (simplification) and model updating process (both procedures are performed simultaneously). Stated another way, the main aim of this work is to develop a SIA strategy for offshore jacket ‐ type structures based on the FE model updating and a novel simplified technique which is less sensitive to both measurement and model uncertainties. RSM scheme can brings about a fast damage zone identification process and also, this simplification leads to a reduction in amount of calculations and expenses. The results demonstrate that the proposed methods provide reliable assesses of damage utilizing the measured incomplete modal data.

The Model Updating and Simplification Approach

Measured FRFs and mode shapes have been applied in FE model updating, by utilizing their features. Updating applying measured FRFs conquers both the problem caused by insufficient information, as measured information can be obtained at any number of frequency points, and the problem of introducing additional inaccuracies from modal analysis, as the measured FRF information are utilized directly. Also, the FRFs contain damping characteristics that otherwise have to be modeled when applying the measured modal properties approach. Another benefit of exploiting and applying measured FRF directly is that no pairing or matching of mode shapes is necessary [14]. The dynamic response of a multi degree damped structural system by a second-order matrix differential equation given by:

$$[M]\{\ddot{U}\}+[C]\{\dot{U}\}+[K]\{U\}=\{Q(t)\} \quad (1)$$

Where $[M]$, $[C]$ and $[K]$ stand for mass matrix, damping matrix and stiffness matrix, respectively. Also, $\{U(t)\}$, $\{\dot{U}(t)\}$ and $\{\ddot{U}(t)\}$ represent the nodal displacement, velocity and acceleration vectors of the structure, respectively. Furthermore, $\{Q(t)\}$ is the forcing function vector. The damping matrix is assumed to be proportional and is defined in terms of mass and stiffness matrices as follows:

$$[C]=\chi[M]+\gamma[K] \quad (2)$$

Equation (1) could be rewritten as follows:

$$[M]\{\ddot{U}\}+[C]\{\dot{U}\}+[K]\{U\}-\{Q(t)\}=\{0\} \quad (3)$$

If it is presumed that:

$$\{U\}=\{U(\omega)\}e^{i\omega t} \quad (4)$$

By taking the appropriate derivatives, we have:

$$\{\dot{U}\}=i\omega\{U(\omega)\}e^{i\omega t} \quad (5)$$

$$\{\ddot{U}\}=-\omega^2\{U(\omega)\}e^{i\omega t} \quad (6)$$

Substituting Equations (5) and (6) into Equation (3), the equation may be presented in the frequency domain as follows:

$$\left(-\omega^2[M]+i\omega[C]+[K]\right)\{U(\omega)\}-\{Q(\omega)\}=\{0\} \quad (7)$$

$$[Z(\omega)]\{U(\omega)\}-\{Q(\omega)\}=\{0\} \quad (8)$$

In Equation (8), $[Z(\omega)]$ is the dynamic stiffness matrix of the structure. In Equation (7), $\{U(\omega)\}$ and $\{Q(\omega)\}$ are measured quantities. The drawback with Equation (7) is that FRFs are measured, instead of individual displacements and force. To fix this drawback, the excitation/ stimulation is presumed to be white noise, and hereupon the vector $\{Q(\omega)\}$ has a unit force magnitude at all frequencies, and the displacement is replaced by the FRFs. If the measured FRFs are applied into Equation (3), utilizing $[M]$, $[C]$ and $[K]$ from the FE model, then there will be an error that will depend on the accuracy of the FE model. This system error vector may be presented on the right hand side of Equation (8) and the resulting equation is:

$$[Z(\omega)]\{U(\omega)\}-\{Q(\omega)\}=\{\Omega(\omega)\} \quad (9)$$

Because of the difficulty in the check of the elements of the error vector, the Euclidean norm (Δ), which is the square root of the sum of the squares of the error vector elements, is utilized [15]. If the error vector has zero elements, then (Δ) will be equal to zero. The equation for Δ is:

$$\Delta = \left(\sum_{i=1}^{\eta} \left| \Omega(\omega_i)^2 \right| \right)^{0.5} \quad (10)$$

Where, η is the number of frequency points. The structural element stiffness, mass, and damping matrices depend on the area (A), density (ρ), Poisson ratio (ν) and the modulus of elasticity (E) of each element. By changing one of these physical parameters, Δ can be minimized. The A, ρ, ν and E acquired by updating the FE model are thus known as updating parameters. A simplified platform model that represents the dynamic properties of jacket platform model and effectively reduces the computational effort has the potential to facilitate the structural damage detection steps. Hereof, there has been no research/ or work directly focusing on the damage detection based on simplified platform model as the main scope of the study. Although limited researchers have conducted studies on establishing simplified models for analysis and performance evaluation of the jacket platform [16, 17]. Accordingly, the reflection of model simplification effects on the dynamic performance of the jacket platform is considered as a perspective of this work for improving a SIM strategy for jacket structures based on the FE model updating. This simplification leads to a reduction in amount of calculations and expenses. For instance, many members of the initial platform model are replaced by a member in the simplified platform model, as shown in Figure 1. By imposing desired technique (FRT), a full accordance between the dynamic properties in both empirical and simplified model is gained. In other words, we introduced the novel simplified method (RSM) in both model reducing (simplification) and model updating process (both procedures are performed simultaneously), which is inspired by the computational intelligence algorithm. Based on the proposed scheme, new members created to be replaced in the desired position. Accordingly, properties of the removed members; including stiffness and mass features are equivalent to properties of the replaced members. Eventually, the RSM is produced.

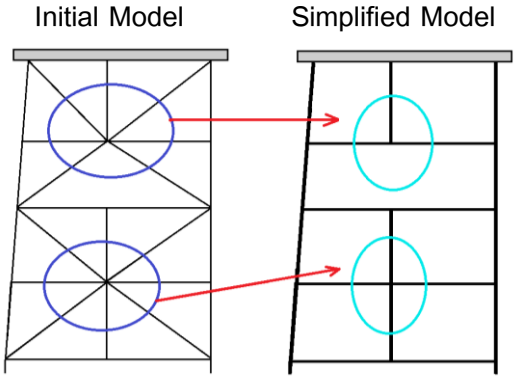

Figure 1: A diagrammatic sketch for creating a simplified platform model.

CMCM Method and Improved Reduction Algorithm Due to Incomplete Modal Data

The main framework of the algorithms being used in this study is based on the structure of the approach similar to CMCM [18]. In this section, this method introduce briefly. The eigensolution of the target system consists of the eigenvalues and eigenvectors. The ith eigenvalue and eigenvector associated with *K* and *M* is expressed as:

$$K\Phi_i = \lambda_i M \Phi_i \quad (11)$$

Where M and K is the mass matrix and stiffness matrix for the undamaged model and λ_i and Φ_i is the ith eigenvalue and eigenvector associated with *K* and *M*. In the development of the CMCM method, it is assumed that the stiffness and mass matrices of the structure denoted by *K* and *M* are obtained from a finite element model. Assume that the stiffness matrix K^* of the actual (experimental) model is a modification of *K* to be formulated as:

$$K^* = K + \sum_{n=1}^{N_e} \alpha_n K \quad (12)$$

Where K_n is the stiffness matrix corresponding to the nth element, N_e is the number of elements, and α_n are unknown correction factors to be determined. Herein, for simplicity in presentation, it is assumed that each element involves a parameter to be updated, such as the Young's modulus of each element. In most studies for the damage detection, particularly in relation to offshore structures usually changes in the mass matrix are negligible.so, it is assumed that:

$$M = M^* \quad (13)$$

Express the jth eigenvalue and eigenvector associated with K^* and M^* as:

$$K^* \Phi_j^* = \lambda_j^* M^* \Phi_j^* \quad (14)$$

It is assumed that a few of λ_j^* and Φ_j^* are known measurements available from modal testing. Premultiplying Equation (14) by $(\Phi_i)^t$ yields:

$$(\Phi_i)^t K^* \Phi_j^* = \lambda_j^* (\Phi_i)^t M^* \Phi_j^* \quad (15)$$

Where the superscript ''t'' is the transpose operator. Substituting Equations (12) and (13) into Equation (15) yields:

$$C_{ij}^{\int} + \sum_{n=1}^{N_e} \alpha_n C_{n,ij}^{\int} = \lambda_j^* \left(D_{ij}^{\int} \right) \quad (16)$$

After using a new index v to replace *ij*, Equation (16) becomes:

$$C_{v}^{\int} + \sum_{n=1}^{N_e} \alpha_n C_{n,v}^{\int} = \lambda_j^* \left(D_{v}^{\int} \right) \quad (17)$$

Where $C_{n,v}^{\int} = (\Phi_i)^t K_n \Phi_j^*$, $C_v^{\int} = (\Phi_i)^t K \Phi_j^*$ and $D_v^{\int} = (\Phi_i)^t M \Phi_j^*$. Rearranging Equation (17), one obtains:

$$\sum_{n=1}^{N_e} \alpha_n C_{n,v}^{\int} = f_v^{\int} \quad (18)$$

Where, $f_v^{\int} = -C_v^{\int} + \lambda_j^* D_v^{\int}$. When N_i modes are taken from the analytical (baseline) finite element model, and N_j modes are measured from the damaged structure, totally $N_v = N_i \times N_j$ equations can be formed from Equation (18). Equations formed based on Equation (18) are named CMCM equations because they involve two modes of two models. Rewriting Equation (18) in a matrix form, one shows:

$$C_{N_v \times N_e}^{\int} \alpha_{N_e \times 1} = f_{N_v \times 1} \quad (19)$$

When N_v is greater than N_e, a least-squares technique can be taken to expect for α.

$$\alpha = \left(C^t C\right)^{-1} C^t f^{\int} \quad (20)$$

One of the simplest reduction schemes is static reduction (Guyan). The full scale model may have certain nodal freedoms specified as master freedoms. The remaining freedoms are slave freedoms. For dynamic analysis purposes the mass, stiffness and loading on the slave freedoms are condensed to these master freedoms. In matrix notation the overall matrices may be partitioned into master, slave and cross coupling terms.

$$\begin{bmatrix} [M_{mm}] & [M_{ms}] \\ [M_{sm}] & [M_{ss}] \end{bmatrix} \begin{Bmatrix} \ddot{U}_m \\ \ddot{U}_s \end{Bmatrix} + \begin{bmatrix} [K_{mm}] & [K_{ms}] \\ [K_{sm}] & [K_{ss}] \end{bmatrix} \begin{Bmatrix} U_m \\ U_s \end{Bmatrix} = \begin{Bmatrix} 0 \\ 0 \end{Bmatrix} \quad (21)$$

Where, the subscripts m and s refer to the master and slave coordinates, respectively. The technique then ignores the inertia terms in the second set of Equations. Neglecting the inertia terms for the second set of equations we have:

$$[K_{sm}]\{U_m\} + [K_{ss}]\{U_s\} = [T_s]\{U_m\} \quad (22)$$

By eliminating the slave DOF, we obtain:

$$\begin{Bmatrix} U_m \\ U_s \end{Bmatrix} = \begin{bmatrix} [I] \\ -[K_{ss}]^{-1}[K_{sm}] \end{bmatrix} \{U_m\} = [T_s]\{U_m\} \quad (23)$$

T_s is Guyan transformation matrix and I is identify matrix. The reduced Guyan mass and stiffness matrices are then given by [19]:

$$[M_R] = [T_s^T][M][T_s] \quad (24)$$

$$[K_R] = [T_s^T][K][T_s] \quad (25)$$

For larger marine structures, where it is necessary to reduce many slave DOF, this technique will not be as accurate as some of the more advanced approaches. Accordingly, improved reduction skill is probably the best practical process for solving large dynamic problems. Only the smallest frequencies are usually excited and for a typical jacket no more than 30 would normally be required. The process known as the Improved Reduction System (IRS) was presented by O'Callahan in 1989 [20]. This technique is an improvement over the Guyan static reduction scheme via introducing a term that includes the inertial effects as pseudo static forces. A transformation matrix T_i is applied to reduce the mass and stiffness matrices. It is defined as:

$$[T_i] = [T_s] + [S][M][T_s][M_R^{-1}][K_R] \quad (26)$$

$$S = \begin{bmatrix} [0] & [0] \\ [0] & [K_{SS}^{-1}] \end{bmatrix} \quad (27)$$

M_R and K_R are the statically reduced mass and stiffness matrices. The new reduced mass and stiffness matrices can be obtained by:

$$[M_{IRS}] = [T_i^T][M][T_i] \quad (28)$$

$$[K_{IRS}] = [T_i^T][K][T_i] \quad (29)$$

For this process, the rows and columns corresponding to the slave coordinates are eliminated from the mass and stiffness matrices one at a time; this allows the mass and stiffness matrices to adapt to the removal of a slave, and can possibly alter the DOF that will be removed. After each reduction, the DOF with the lowest K_{ii}/M_{ii} term is the slave which will be eliminated next [21].

Physical Model and Test Set up

A physical model was constructed of steel pipes that were welded together using argon arc welding to ensure proper load transfer. The experimental model is built of steel tubes, utilizing $34mm \times 3.5mm$ (outer diameter and thickness) section as 2 legs and $21mm \times 2.0mm$ section as all braces, and box cross section at the top with $40mm \times 20mm$ and $2mm$ thickness to simulate the upside structure. The 2D steel frame model structure has dimensions of $560mm$ (on the bottom) and $480mm$ (on the top) in width and has heights of $280mm, 285mm, 270mm$ and $270mm$ at the 1st, 2nd, 3rd and 4th storey, respectively, giving a total height of $1105mm$. The physical model along with test rig and FE model of the laboratory tested 2D steel frame jacket structure adopted for model updating is shown in Figure 2. The FE model presented in Figure 2 has 15 nodes and 29 elements with a total number of 45 degrees of freedoms. The mass density of the members is 7850 kg/m3 and the Young's modulus of steel is 207 GPa. The white noise signals were used as the input exciting signal. The instrumentation included two light uniaxial accelerometers (4508 B&K) in both the X and Y directions on each joint for response measurement and a load cell for measuring

the excitation force. The frequency sampling of the test setup was chosen to be 10 kHz, and the frequency range was 0-200 Hz. The recorded data were sent to the PULSE [22] software package for processing. The data required for calculating the FRFs were recorded by sensors that were fixed on the physical model joints. First tests are done on the undamaged structure. Then the tests are repeated in the same way for the damaged structure by removing the member of the model, as shown Figure 3.

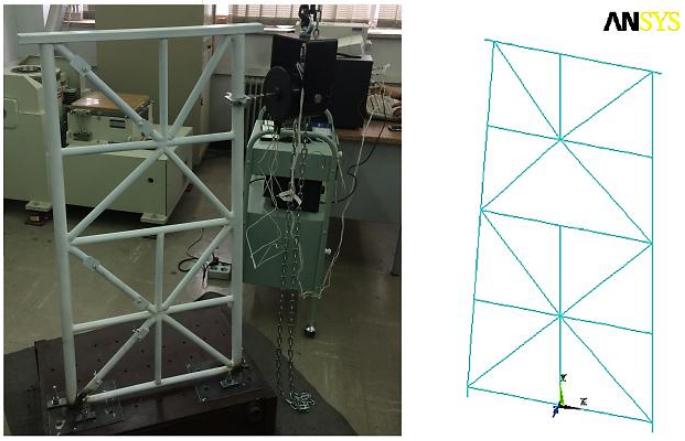

Figure 2: The physical model and FE model

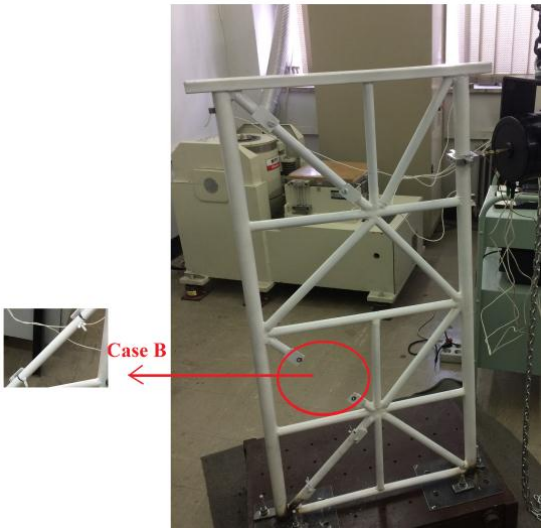

Figure 3: Experimental damage scenarios

Results and discussion

Refined simplified FE model of platform (RSM)

For production of perfect RSM, the obtained result from solving Equation 10 is presented in Figure 4 and Table 1. Moreover, Figure 5 and Table 2 imply the perfect correlation between the acquired natural frequencies of the RSM and experimental results.

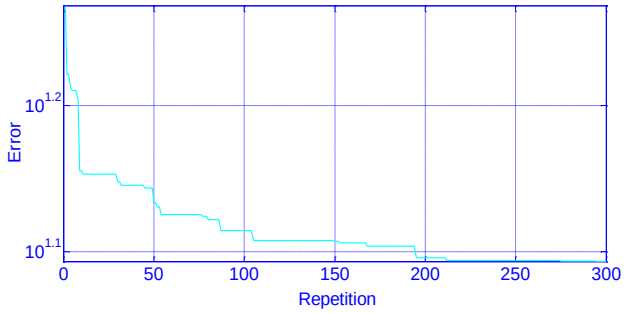

Figure 4: The convergence process obtained from solving the objective function.

Table 1: The obtained result from solving the objective function

Area	A_1	A_2	A_3	A_4	A_5	A_6	A_7	A_8
(cm^2)	11.61	6.02	3.461	11.61	5.53	6.02	5.33	6.72
Moment of inertia	I_1	I_2	I_3	I_4	I_5	I_6	I_7	I_8
(cm^4)	28.531	17.496	4.35	28.531	13.496	17.469	15.765	19.113

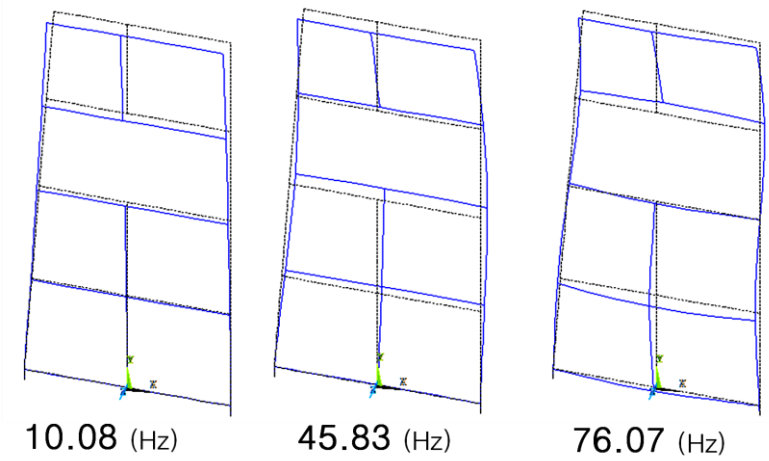

Figure 5: The first three mode shapes of the RSM.

Table 2: The first four natural frequencies.

Mode No.	1st	2nd	3rd	4th
Initial Model	16.49 (Hz)	58.03 (Hz)	91.75 (Hz)	143.25 (Hz)
Empirical Model	9.8 (Hz)	45.3 (Hz)	75.8 (Hz)	145 (Hz)
RSM	10.08 (Hz)	45.83 (Hz)	76.39 (Hz)	144.53 (Hz)

The updating and refining of the original FE model is required to minimize the numerical model error according to the experimental signatures. The ideas of the "*Modal Assurance Criterion*" (***MAC***) approach can be employed for this intention. A typical correlation criterion is the MAC which gives a single value between 0 and 1 for the mode shape concurrence. The MAC, between analytical mode φ_i and experimental mode φ_j is expressed as:

$$MAC(\varphi_i,\varphi_j)=\frac{|\varphi_i^T\varphi_j|^2}{(\varphi_i^T\varphi_i)(\varphi_j^T\varphi_j)} \qquad (30)$$

Based on this factor, the MAC values always lie between 0 and 1, where values closer to 1 indicate a better agreement between the considered mode shapes. Results imply that the MAC values between the mode shapes of the RSM and the mode shapes of the tested physical model are all greater than 0.94, which represents that an effective RSM has been produced. The damaged structure has three damage elements, including element ***A***, ***B*** and ***C*** (see Figure 6). For instance, element ***B*** in the damaged structure is equivalent with damage in "*Zone* 3" located in the RSM.

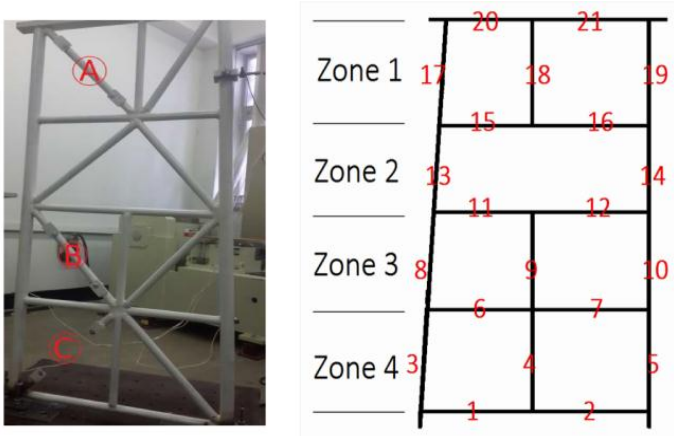

Figure 6: RSM and damaged model along with the locations of the damaged members and element number.

Damage detection using RSM

In the present work, damage identification strategy is applied on three damage cases to illustrate the applicability of the proposed technique for jacket structures. Three experimental tests were performed based on the exhibited scenarios in Figure 6. Damage identification results utilizing refined simplified FE model (RSM) and improved model reduction approach is shown in Figure 7 for case *B*.

As the first step, a without-iteration procedure is employed $(T=T^*)$ and also, the damage assessment utilizing only the three modes of the damaged model is checked. Shown in Figure 7 is the damage severity for case *B* when only the first three mode shapes of the damaged model are applied. Several members of the platform model as shown in Figure 7(a), are poorly estimated. In the next step, the iterative procedure is employed, T^* is always computed using the damaged model acquired from the previous

iteration. So, employing the RSM and iterations develops the performance of the SIA process. Clearly, Member "9" of the refined simplified FE model represents the probable damage for members located on "*Zone* 3" of the damaged jacket platform (see Figure 6).

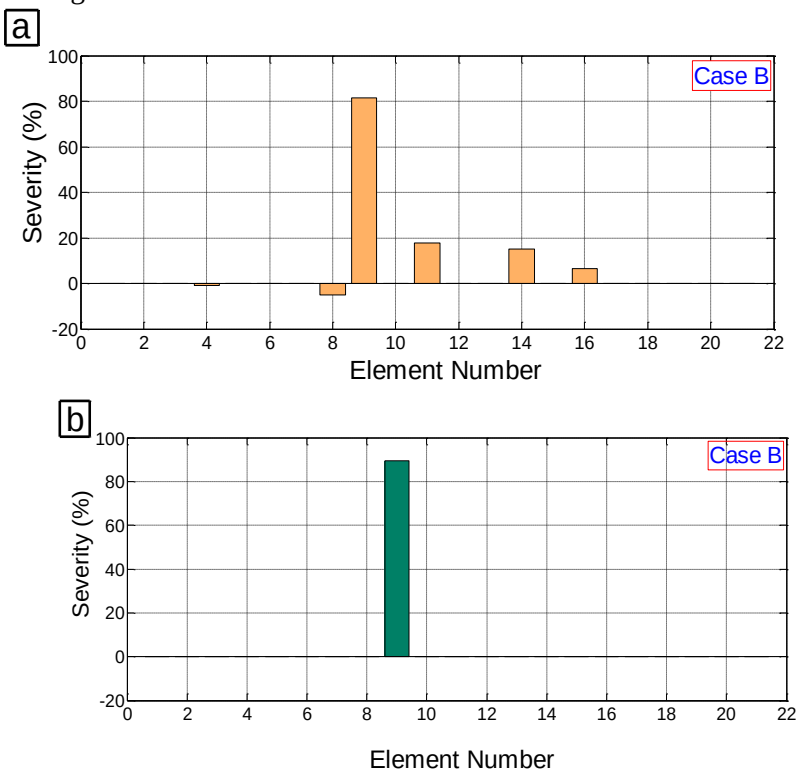

Figure 7: Damage detection results using RSM and improved model reduction approach: (a) without iteration (b) with iteration for case *B*.

Conclusions

This work develops a robust simplified method for SIM of offshore platform structures. Aiming at the restriction of the original CMCM method, which only uses baseline FE model; this study provides a useful damage diagnosis process by introducing a novel simplified methodology and successfully acquired damage indicator by using RSM. The first four natural frequencies which are acquired from the experimental modal analysis are 9.8, 45.3, 75.8 and 145 Hz, respectively, and after production of the RSM based on FRT and CI algorithm, the MAC factor to verify adjustment mode shapes obtained from RSM with mode shapes obtained from empirical model is also employed. In addition to elimination of uncertainty effects in the damage detection results, RSM technique is used due to practical considerations and also this technique provides a fast damage zone detection process. For the implementation of the proposed SIM technique, an improved reduction scheme (static reduction) is also applied to damage diagnosis procedure. This scheme removes the bad effect of model reduction process and prevents the appearance of spurious modes on the proposed SIA method. The findings of the study revealed that the proposed methodology is effective, practical and useful in the damage diagnosis of fixed offshore platforms.

List of Symbols

RSM	Refined Simplified Model
SIA	Structural integrity assessment
SIM	Structural integrity monitoring
CMCM	Cross model cross mode
FE	Finite element model
CI	Computational intelligence
DOF	Degrees of freedom

References

[1] Asgarian, B., Aghaeidoost, V., Shokrgozar, H.R., "Damage detection of jacket type offshore platforms using rate of signal energy using wavelet packet transform", Marine Structure, Vol. 45, pp. 1-21, 2016.

[2] Wang, S.H., "Damage detection in offshore platform structures from limited modal data", Applied Ocean Research, Vol. 41, pp. 48-56, 2013.

[3] Caines, S., Khan, F., Shirokoff, J., Qiu, W., "Experimental design to study corrosion under insulation in harsh marine environments", Loss Prevention in the Process Industries, Vol. 33, pp. 39-51, 2015.

[4] Tang, Y., Qing, Z.H., Zhu, L., Zhang, R., "Study on the structural monitoring and early warning conditions of aging jacket platforms", Ocean Engineering, Vol. 101, pp. 152-160, 2015.

[5] Kuang, K.S.C., "Distributed damage detection of offshore steel structures using plastic optical fibre sensors", Sensors and Actuators, Vol. 229, pp. 59-67, 2015.
[6] Ji, C.Y., Xue, H.Z., Shi, X.H., Gaidai, O., "Experimental and numerical study on collapse of aged jacket platforms caused by corrosion or fatigue cracking", Engineering Structures, Vol. 112, pp. 14-22, 2016.
[7] Ren, W.X., Sun, Z.S., Xia, Y., Hao, H., Deeks, A.J., "Vibration-based damage identification of shear connectors in bridge decks: laboratory test study", Journal of Structural Engineering, Vol. 134, pp. 832-841, 2008.
[8] Chakraborty, S., Sen, A., "Adaptive response surface based efficient finite element model updating", Finite Elements in Analysis and Design, Vol. 80, pp. 33-40, 2014.
[9] Yuan, X.Z., Yu, K.P., "Finite element model updating of damped structures using vibration test data under base excitation", Journal of Sound and Vibration, Vol. 340, pp. 303-316, 2015.
[10] Kianian, M., Golafshani, A.A., Ghodrati, E., "Damage detection of offshore jacket structures using frequency domain selective measurements", Marine Science and Application, Vol. 12, pp. 193-199, 2013.
[11] Kaveh, A., Zolghadr, A., "An improved CSS for damage detection of truss structures using changes in natural frequencies and mode shapes", Advances in Engineering Software, Vol. 80, pp. 93-100, 2015.
[12] Kuang, K.S.C., "Distributed damage detection of offshore steel structures using plastic optical fibre sensors", Sensors and Actuators, Vol. 229, pp. 59-67, 2015.
[13] Farrar, C.R., Worden, K., "An introduction to structural health monitoring", Phil. Trans. R. Soc. A, Vol. 365, pp. 303-315, 2007. (doi:10.1098/rsta.2006.1928)
[14] Marwala, T., "Finite-element-model updating using computional intelligence techniques: Applications to structural dynamics", Springer London Dordrecht Heidelberg New York., 2010. (DOI 10.1007/ 978-1-84996-323-7)
[15] Farrar, C.R., Worden, K., "An introduction to structural health monitoring", Phil. Trans. R. Soc. A, Vol. 365, pp. 303-315, 2007. (doi:10.1098/rsta.2006.1928)
[16] Park, M., Koo, W., Kawano, K., "Dynamic response analysis of an offshore platform due to seismic motions", Engineering Structures, Vol. 33, pp. 1607-1616, 2011.
[17] Zhou, B., Han, X., Tan, S.K., "A simplified computational method for random seismic responses of a jacket platform", Ocean Engineering, Vol. 82, pp. 85-90, 2014.
[18] Hu, S.L.J., Li, H., Wang, S.H., "Cross-model cross-mode method for model updating", Mechanical Systems and Signal Processing, Vol. 21, pp. 1690-1703, 2007.
[19] Guyan, R.J., "Reduction of stiffness and mass matrices", AIAA Journal, Vol. 3(2), p. 380, 1965.
[20] Friswell, M.I., Mottershead, J.E., "Finite element model updating in structural dynamics", Kluwer Academic Publishers, 1995.
[21] Barltrop, N.D.P., Adams, A.J., "Dynamics of fixed marine structures", Butterworth-Heinemann, Oxford, Third edition, 1991.
[22] PULSE. Analyzers and solutions, release 11.2., "Denmark: Bruel & Kjaer", Sound and Vibration Measurement A/S. Key code: 232072F0, 2006.

INTERNATIONAL JOURNAL OF
COASTAL & OFFSHORE ENGINEERING
IJCOE No. 2/Spring 2016 (17-22)

Surveying sea surface effect in satellite altimeter-derived wind speed

Hossein Farjami[1], **Pavel Golubkin**[2], **Bertrand Chapron**[3]

[1]*Iranian National Institute for Oceanography and Atmospheric Science, IRAN*
[2]*Satellite Oceanography Laboratory, Russian State Hydrometeorological University, St. Petersburg, Russia,*
[3]*Laboratoire d'Oceanographie Spatiale, Ifremer, Plouzane, France*

ARTICLE INFO

Article History:
Received: 3 May. 2016
Accepted: 15 Jun. 2016

Keywords:
wind speed, satellite altimeter, coastal regions

ABSTRACT

To improve sea surface wind speed in coastal regions, we used nadir satellite altimeter measurements in the Persian Gulf and Arabian Sea. With combining normalized radar cross section for two bands of satellite altimeter measurements and significant wave height suggested the method to obtain "true" sea surface wind speed. In the coastal regions, we used a dimensionless significant wave height to gain empirical dependency to fetch-limited wind wave development. In this research, normalized radar cross section is simulated by using inverse wave age and fetch laws. As established this method helps to refine altimeter measurements of sea surface wind in the coastal regions.

1. Introduction

Satellite altimeters provide sea surface height and synchronous measurements of normalized radar cross section(NRCS) and significant wave height(Hs) in the oceans that related to sea surface state[1]. Most observations and analysis using global sampling of dual-frequency altimeters, i.e. since TOPEX measurements [2, 3], use both C- and Ku-band along with Hs estimates, and suggest means to better isolate the short-scale wind-related information contained in the differing NRCS measurements from the longer energy-containing scales [4, 5]. To better estimate of short surface wave scales by satellite altimeter measurements, we can use dual-frequency altimeter measurements. This waves directly related to physical air-sea processes, such as the local wind stress and the rate of gas exchange across the sea surface [6]. Elfouhaily et al. (1998) first proposed a theoretical method to estimate surface wind speed (U_{10}) from linear combinations of Ku- and C-band NRCS measurements of the TOPEX dual-frequency altimeter data. As demonstrated, the dual-frequency capability convincingly improves friction velocity estimation for wind speed higher than 7 m/s. Comparing with buoy data, the retrieved wind speed by a dual-frequency instrument was equally improved compared to a mono-frequency capability [4].

In this research, suggested the method to improve altimeter measurements of sea surface wind speed using nadir dual-frequency altimeter normalized and significant wave height measurements in the coastal areas, more precisely over the Persian Gulf and Arabian Sea. For our purpose, we use the Ocean Surface Topography Mission (OSTM)/Jason-2 and Jason-1 altimeter data. Of particular interest over coastal regions, the joint evolution of NRCS and Hs measurements can be analyzed and interpreted using fetch-limited laws to take into account possible rapid wind wave development [7, 8, 9].

Data and Methodology

The Ocean Surface Topography Mission on the Jason-2 satellite (OSTM/Jason-2) is a follow-on to the Jason-1 mission. It was launched in June 2008 in the frame of cooperation between National Aeronautics and Space Administration (NASA), European Organization for the Exploitation of Meteorological Satellites (Eumetsat), Centre National d'Etudes Spatiales (CNES), and National Oceanic and Atmospheric Administration (NOAA) with aims to continue high quality measurements of ocean parameters and to provide operational products to modeling and forecasting applications[10]. Main instrument carried aboard the satellite Jason-2 is Poseidon-3, which is a dual-frequency radar altimeter operating in Ku-band (13.575 GHz) and C-band (5.3 GHz). It has 9.9156 days repeat cycle with sample frequency 1Hz and 20Hz (http://www.aviso.altimetry.fr/). The second frequency is primarily used to provide correction for ionospheric electronic content. The data used in this study are Geophysical Data Records (GDRs) provided by NOAA.

Jason-1 satellite with a nadir-looking dual-frequency radar altimeter onboard was launched in December

2001. It operated with Ku-band and C-band frequencies the same as Jason-2 altimeter.

In the present study, (GDRs) Level-2 sampling from the Physical Oceanography Distributed Active Archive Center (PODAAC) of National Aeronautics and Space Administration (NASA) Jet Propulsion Laboratory (JPL) was used.

Longer waves not fully coupled to the local wind field can effect to altimeter measurements of wind speed[4]. This problem is especially relevant near coastal zones, where rapid wave development can take place under relatively constant offshore wind conditions. Growing waves contribute to broaden the local wind wave spectral range, leading to increase both the mean squared elevations and slopes of the ocean surface [7]. Probed along an altimeter track, such phenomena will thus lead to rapid and opposite Hs and NRCS changes. As a first consequence, derived wind speeds using a standard mono-frequency Ku-band algorithm, are likely to be underestimated [9].

To possibly overcome such a deficiency, Elfouhaily et al. (1998) proposed to analyze a more closely wind-related parameter $\delta\sigma^0_{dB} = (\sigma^0_C)_{dB} - (\sigma^0_{Ku})_{dB}$ to more efficiently isolate the short-scale roughness contribution. Here $(\sigma^0_C)_{dB}$ and $(\sigma^0_{Ku})_{dB}$ are NRCS of C- and Ku band in decibel, respectively, and $\delta\sigma^0_{dB}$ is their difference. Figure 2 (a) shows $(\sigma^0_{Ku})_{dB}$ and $(\sigma^0_C)_{dB}$, and their difference versus wind speed from Geophysical Data Records (*GDRs*) in the North Indian Ocean on 26 January 2013. Under homogenous sea state conditions, Ku- and C-band NRCS decrease with wind speed due to an increase of the surface wave Mean Square Slope (MSS). Not considering calibration issues, C-band NRCS are then expected higher than Ku-band ones, according to two effects: a larger C-band Fresnel coefficient, and a smaller effective MSS, linked to the larger C-band radar wavelength. Using NRCS difference, roughness impact, in the wavenumber interval confined by Ku- and C-band dividing wavenumbers, of order 285.6 and 112.2 rad/m, correspondingly, can be extracted. Since short-scale waves in this interval does not strongly depend on wave age, the use of the difference $\delta\sigma^0_{dB}$ shall be more closely related to wind speed only (see [3] for more details). In coastal regions and/or atmospheric fronts this parameter may thus be used to better interpret if rapid changes in altimeter-derived wind speed are caused by the impact of longer wave development under a relatively constant wind, or by "real" changes in wind speed conditions.

To further derive a more consistent local wind speed under nonhomogeneous conditions, e.g. fetch-limited situations, the altimeter Hs measurement and its evolution can further be considered. For closed-basin conditions over the Arctic area, Golubkin et al. (2014) [9] applied the concept introduced by Kitaigorodskii (1962) [13] to consider the self-similarity of wave development. Accordingly, knowing the distance from shore, the related Hs changes can also directly help to retrieve a wind estimate and the peak period of the developing wind sea. As further promoted by Badulin (2014) [8], a physical model for sea wave period from altimeter data can directly use Hs measurements and along-track spatial derivatives. Indeed, assuming stationary wind conditions, a simplified formulation can be derived from a physical model (Eq 6 in [8]), consistent with empirical fetch laws (see [14] and [15] for further discussions).

To illustrate these fetch-effects, we concentrate our analysis of altimeter measurements in the North Indian Ocean. In this paper, six particular altimeter passes are presented and discussed (Figure 1).

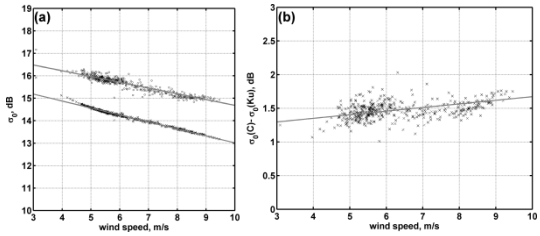

Figure 2. Jason-1 pass 45 on 26 January 2013

in the North Indian Ocean. (a) NRCS versus standard wind speed product for Ku- (crosses) and C-band (circles). (b) Difference between C-band and Ku-band NRCS. Gray lines show linear fit to the data

According to simplified physical optics or Kirchhoff approximation, we can estimate NRCS of satellite altimeter [2, 16]:

$$\sigma^0_{em}(0^\circ) = \frac{|R_0|^2}{MSS}\exp(-4k_r^2 h_s^2) \tag{1}$$

where R_0 is nominal Fresnel coefficient and $\exp(-4k_r^2 h_s^2)$ is a correction to the Geometrical Optics (GO) scattering approximation to take into account small (compared to the facet size) scale roughness impact, where k_r is radar wavenumber, h_s^2 the small scale variance in the wavenumber range $k > k_d$. The MSS and h_s^2 are calculated via wave spectrum as

$$MSS(\alpha, U_{10}, k_r) = \int_0^{k_d} B_0(\alpha, U_{10}, k)\, d\ln k \tag{2}$$

$$h_s^2 = \int_{k_d}^{\infty} k^{-2} B_0(\alpha, U_{10}, k)\, d\ln k \tag{3}$$

where k is wavenumber, B_0 is the omnidirectional wave saturation spectrum. U_{10} is wind speed at 10 m reference level, g is the gravitational acceleration, $\alpha = k_p^{1/2} U_{10} g^{-1/2}$ is the inverse wave age. Following a

2-scale PO scattering approximation, k_d corresponds to a typical scale linked to the facet size providing radar returns. For the sake of the demonstration, this typical scale is here taken as four times the radar wavelength. In the present study, we use the spectrum suggested by [17] with the following fetch law for inverse wave age:

$$\alpha = 0.84 \times \left\{ \tanh(\tilde{x} / \tilde{x}_0)^{0.4} \right\}^{-0.75} \quad (4)$$

Correspondingly, the integral over the wave spectrum provides the following fetch law for the dimensionless Hs:

$$\tilde{H}_s = 0.26 \times \tanh\left\{ \left(\tilde{x} / \tilde{x}_0 \right)^{0.4} \right\}^{1.25} \quad (5)$$

where $\tilde{x}$ is dimensionless fetch, $\tilde{x}_0 = 2.2 \times 10^{-4}$ and $\tilde{H}_s = H_s g / U_{10}^2$.

To help assess the interpretation of the observed NRCS changes along the altimeter tracks for the analyzed cases, we simulate NRCS, Eq. (1), taking into account the degree of development (wave age) via Eq. (4) for each fetch x. As an alternative, at each altimeter measurement, the inverse wave age, $\alpha = k_p^{1/2} U_{10} g^{-1/2}$, is evaluated using the altimeter Hs measurements from the relation (which follows from (4) and (5):

$$\alpha = 0.84 \times \left(\frac{\tilde{H}_s}{0.26} \right)^{-0.6} \quad (6)$$

The results of NRCS simulation are reported in Figure 3. The NRCS (Ku-band) is estimated for different wind speeds (5 m/s, 10 m/s, 15 m/s) as function of Hs. Very low Hs would thus correspond to very young sea states. To compare, the two-parameter model, NRCS(U10, Hs), proposed by[4], is also applied. As found, this two-parameter model seems to apply for relatively mature sea state conditions. For very young sea state conditions, it fails to reproduce the possible large NRCS increase. Correspondingly, altimeter wind speed will likely be underestimated. Accordingly, a more direct use of altimeter (NRCS, Hs) estimates and the corresponding joint (but opposite) NRCS and Hs gradients along the altimeter-track must be considered to help further constrain the estimation of the local wind speed and sea state degree of development.

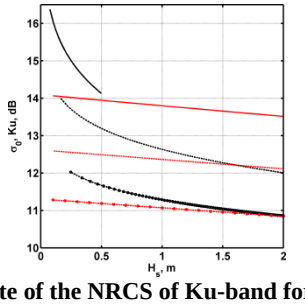

Figure 3. Estimate of the NRCS of Ku-band for wind speeds 5 m/s (solid line), 10 m/s (dashed line), 15 m/s (dash-dot line) as function of Hs. Black line calculated using model spectrum and red line calculated correspond to [4] algorithm.

Analysis and Results

In this part, different typical situations are reported to illustrate fetch-limited effects on satellite altimeter measurements. Jason-1 pass 45, January 26th 2013, is analyzed in the Arabian Sea from Kathiawar peninsula. In this case, the wind blows from coast and its direction is approximately aligned with the altimeter track. Figure 4 shows the evolution of Hs along the first 38 points from the coastline, corresponding to approximately 220 km between the first and the last measurements. Over this distance, the Hs grows from 0.5 m to approximately 1.5 meter (Figure 4a). Both Ku- and C-band NRCS also decrease with fetch. As expected, the altimeter wind speed derived from Ku-band NRCS is then constantly increasing with the distance from coast. However, the difference between C-band and Ku-band NRCS is found almost constant all along this altimeter segment (Figure 4b). As discussed above, this fact indicates that the wind speed is also likely constant (9.5 m/s) along the track, and the increase of altimeter wind speed results from the wave development.

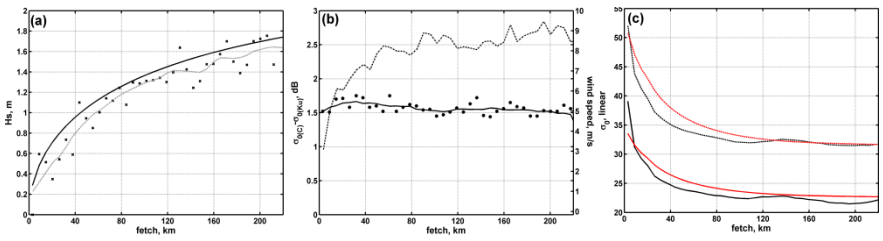

Figure 4. Jason-1 pass 45 on 26 January 2013 in the study region. (a) Hs measured by altimeter (symbols), smoothed Hs (dashed line) and calculated by using fetch law, Eq. 4, (solid line). (b) Difference between C-band and Ku-band NRCS (symbols) and their smoothed (solid line) and corresponding wind speed from the standard altimeter product (dashed line, right axis). (c) Smoothed NRCS measured by altimeter (black solid line for Ku-band and black dashed line for C-band) and calculated using model spectrum (red solid line for Ku-band and red dashed line for C-band), NRCS of model spectrum multiplied to 1.3 (for C-band) and 1.4 (for Ku-band) to fit with NRCS of altimeter measurement

Another example, on March, 17th 2014, Jason-2 pass 66 also captured a wave development condition in the Arabian Sea. Measurements are reported, Figure 5. In this case, the distance between the first and the last measurements corresponds to 180 km. Hs grows from 0.6 to 1.3 meters (Figure 5a) and the NRSC continuously drops over this interval. The standard altimeter wind speed thus increases from 4 to 8.4 m/s. The difference between NRCS for Ku- and C-band stays almost constant at 1.6 dB. As inferred using the fetch law, a 8.5 m/s constant wind speed can well describe the observed wave development.

On January 14th, 2010, Jason-1 pass 29, the altimeter wind speed increases from 5 to 8 m/s, over the 150 km segment. NRCS difference between Ku- and C-band ones is practically constant at 1.5 dB (Figure 6b). Hs grows from 0.6 to 1.6 meters, and using a constant wind speed 9.5 m/s can help interpret the measurements (Figure 6a).

On December 4th, 2010, Jason-1 pass 207, over 200 km, the difference between NRCS of Ku- and C-band measurements is almost constant, 1.5 dB, and Hs grows from 0.5 to 1.4 m (Figure 7a). Using a constant wind speed, 8.5 m/s, is then found to explain the altimeter observations.

Figure 8 and Figure 9 present two more examples to confirm the impact of wave development on altimeter measurements.

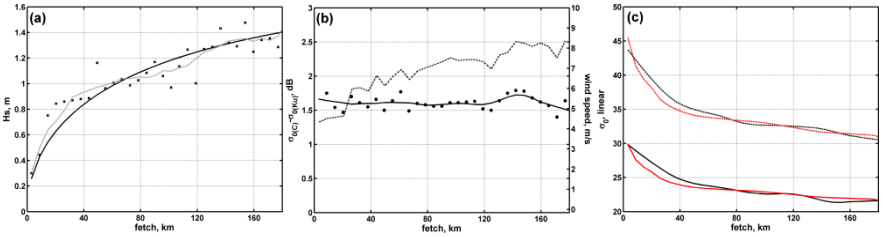

Figure 5. Same as in Figure 4 for Jason-2 pass 66 on 17 March 2014.

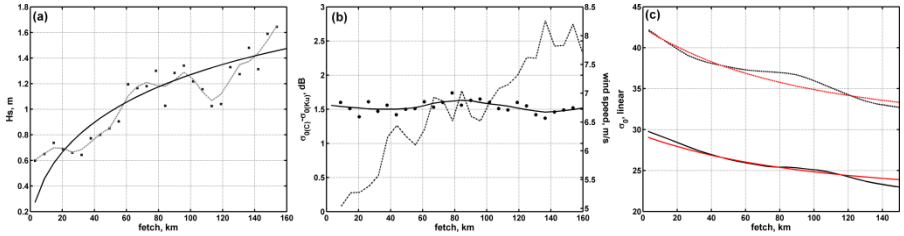

Figure 6. Same as in Figure 4 for Jason-1 pass 29 on 14 January 2010.

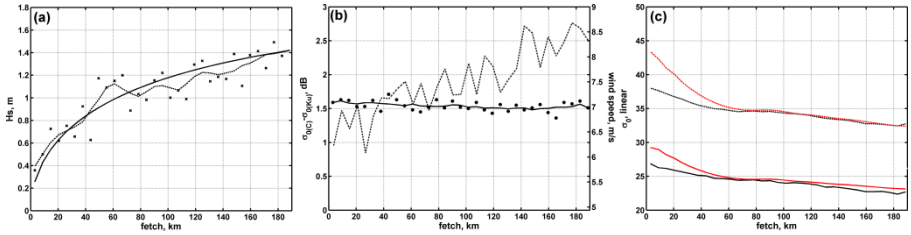

Figure 7. Same as in Figure 4 but for Jason-1 pass 207 on 4 December 2010.

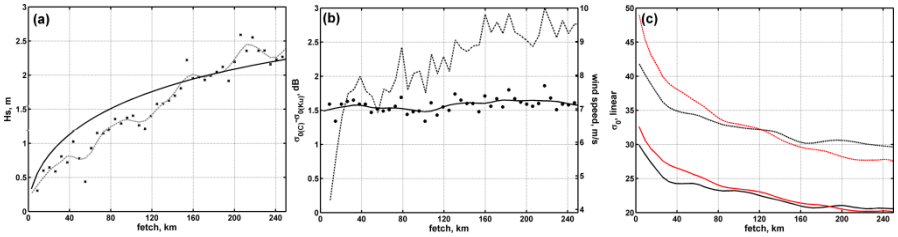

Figure 8. Same as in Figure 4 for Jason-1 pass 244 on 18 February 2005.

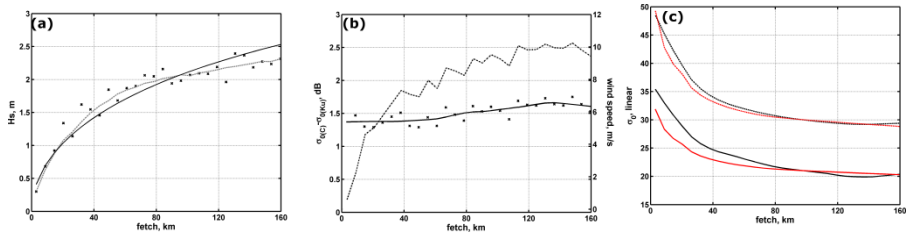

Figure 9. Same as in Figure 4 for Jason-1 pass 105 on 1 February 2004.

Discussion

As demonstrated, wind seas developing for these different cases seem to provide to broaden the local wind wave spectral range, leading to increase both the mean squared elevations and slopes of the ocean surface. From the different reported examples, the simplified NRCS model, Eq.(1), improved with Elfouhaily spectrum [17] with fetch laws (4) and (5) can reasonably explain the along-track altimeter observations. This approves the essential role of the wave development to interpret altimeter observation in coastal areas. As key to analyze and noticed for all these cases, the NRCS differences between Ku- and C-band, $\delta\sigma^0_{dB}$, take almost constant values along the analyzed altimeter tracks. This is related to the rapid modification of short scale roughness to the wind speed, and the weak impact of the sea state degree of development on this short scale roughness. Thus, a constant wind speed assumption can first be efficiently used for all considered cases, to further exploit the Hs changes to infer the most reasonable wind speed.

Golubkin, and et al. 2014, for closed-basin conditions, simply considered the largest retrieved wind values when using mono-frequency altimeter measurements (e.g., SARAL/AltiKa instrument). Using a dual-frequency instrument, the analysis is more straightforward, and can rely on the joint analysis of $\delta\sigma^0_{dB}$ and the Hs evolution.

Applications of satellite altimetry over the open ocean are certainly well established, but measurements near the coasts or in closed-basins [9], can necessitate more dedicated algorithm developments. This study has emphasized the potential of satellite altimeter measurements to derive more detailed sea state information in coastal regions. Indeed As demonstrated, analysis strategy and model developments can build on the combined the Ku- and C-band radar measurements, their difference, the measured significant wave height parameter and its along-track gradient.

With comparing Ku- and C-band NRCS measurements, along-track gradients and differences, can help to question the altimeter wind speed derived from a standard algorithm [3, 4]. Indeed, especially for coastal regions, when both along-track Ku- and C-band NRCS measurements are found to co-vary without major changes perceived in their differences, this likely indicates evolving sea state conditions. Persuasively, a further analysis of along-track altimeter Hs estimates and gradients can then help to more quantitatively confirm the sea state degree of development.

In this study, such developments of wind-driven waves were analyzed using self-similar wave theory [13, 17]. As expected and established using a simplified physical optics scattering model, NRCS and Hs along-track evolutions shall indeed be anti-correlated under developing sea state conditions. Based on the wave spectrum sea state dependency, simulations have been performed (Figure 3), and an empirical relation can be derived to describe this expected anti-correlation. Also, under stationary conditions, a simplified formulation can then further be derived to more efficiently estimate peak wave period information. Furthermore to the methodology proposed by [8], or the methodology based on empirical relationship [18] applied to assess coastal wave energy resource [19] the present analysis suggests to not only consider dual-frequency NRCS measurements [20], but also to analyze joint NRCS and Hs along-track gradients to more quantitatively constrain the peak wave period information. This subject will be studied in the future.

References

[1] Tournadre, J.; Chapron, B.; Reul, N. High resolution imaging of the ocean surface backscatter by inversion of altimeter waveforms. Journal of Atmospheric and Oceanic Technology, 2011, 28, 1050–1062. http://dx.doi.org/10.1175/2011JTECHO820.1.

[2] Chapron, B.; Katsaros, K.; Elfouhaily, T.; Vandemark, D. A note on relationships between sea surface roughness and altimeter backscatter. Remote Sensing and Global Modelling, 1995, 869-878.

[3] Elfouhaily, T.; Vandemark, D.; Gourrion, J.; Chapron, B. Estimation of wind stress using dual-frequency TOPEX data. Journal of Geophysical Research, 1998, 103, Issue C11, 25101–25108. http://dx.doi.org/10.1029/98JC00193.

[4] Gourrion, J.; Vandemark, D.; Bailey, S.; Chapron, B. Investigation of C-band altimeter cross section dependence on wind speed and sea state. Canadian Journal of Remote Sensing, 2002, vol. 28, issue 3, 484-489, http://dx.doi.org/10.5589/m02-046.

[5] Chen, G.; Chapron, B.; Ezraty, R.; Vandemark, D. A dual-frequency approach for retrieving sea surface wind speed from TOPEX altimetry. J. Geophys. Res., 2002, 107(C12), 322.

[6] Goddijn-Murphy L., Woolf , D.; Chapron, B.; Queffeulou, P. Improvements to estimating the air–sea gas transfer velocity by using dual-frequency, altimeter backscatter. Remote Sensing of Environment, 2013, Volume 139, 1–5. http://dx.doi.org/10.1016/j.rse.2013.07.026.

[7] Vandemark, D.; Chapron, B.; Sun, J.; Crescenti, G. H.; Graber, H. C. Ocean Wave Slope Observations Using Radar Backscatter and Laser Altimeters. J. Phys. Oceanogr., 2004, 34, 2825–2842.

[8] Badulin, S. I. A physical model of sea wave period from altimeter data. Journal Geophysical Research Oceans, 2014, 119, 856–869. http://dx.doi.org/10.1002/2013JC009336.

[9] Golubkin, P. A.; Chapron, B.; Kudryavtsev V. N. Wind Waves in the Arctic Seas: Envisat and AltiKa

Data Analysis. Marine Geodesy, 2014, http://dx.doi.org/10.1080/01490419.2014.990592.
[10] Dumont, J. P. OSTM/Jason-2 Products Handbook. 2015, JPL: STM-29-1237, NOAA/NESDIS: Polar Series/OSTM J400.
[11] Tomczak, M.; Godfrey, J. S. Regional Oceanography: an Introduction", 2nd edition, Elsevier Science Ltd., 2003, Oxford, U. K. ISBN: 817035068, 391pp.
[12] Rodo, X.; Comin, F. Global Climate Current Research and Uncertainties in the Climate System, 2002., Springer, Berlin, 10837865, 286 pp.
[13] Kitaigorodskii, S. A. Applications of the theory of similarity to the analysis of windgenerated wave motion as a stochastic process. Izv. Geophys. Ser. Acad. Sci., USSR 1, 1962, p105-117.
[14] Zakharov, V. E., Badulin, S. I., Hwang, P. A., Caulliez, G. Universality of sea wave growth and its physical roots, J. Fluid Mech., 2015, 780, 503–535, *doi:*10.1017/jfm.2015.468.
[15] Kudryavtsev, V.*;* Golubkin, P.*;* Chapron, B. A simplified wave enhancement criterion for moving extreme events, J. Geophys. Res. Oceans, 2015, 120, 7538–7558, *doi:*10.1002/2015JC011284.
[16] Kudryavtsev, V.; Akimov, D.; Johannessen, J.; Chapron, B. On radar imaging of current features: 1. Model and comparison with observations. J. Geophys. Res., 2005, 110, C07016, http://dx.doi.org/10.1029/2004JC002505.
[17] Elfouhaily, T.; Chapron, B.; Katsaros, K.; Vandemark, D. A Unified Directional Spectrum for Long and Short Wind-Driven Waves. Journal of Geophysical Research, 1997, 102, 15781–96. http://dx.doi.org/10.1029/97JC00467.
[18] Gommenginger, C. P.; Srokosz, M. A.; Challenor, P. G. Measuring ocean wave period with satellite altimeters: A simple empirical model, Geophys. Res. Lett., 2003, 30*(*22*), 2150, doi:*10.1029/2003GL017743.
[19] Goddijn-Murphy, L.; Martín Míguez, B.; McIlvenny, J.; Gleizon, P. Wave energy resource assessment with AltiKa satellite altimetry: A case study at a wave energy site. Geophysical Research Letter, 2015, 42, 5452–5459. http://dx.doi.org/10.1002/2015gl064490.
[20] Quilfen, Y.; Chapron, B.; Collard, F.; Serre, M. Calibration/validation of an altimeter wave period model and application to TOPEX/Poseidon and Jason-1 altimeters, Mar. Geod., 2004, 27*(*3–4*)*, 535–549, *doi:*10.1080/01490410490902025.

INTERNATIONAL JOURNAL OF
COASTAL & OFFSHORE ENGINEERING
IJCOE Vol.1/No. 2/Spring 2016 (35-42)

In-Place Strength Evaluation of Existing Fixed Offshore Platform Located in Persian Gulf with Consideration of Soil-Pile Interactions

Rasoul Sadian[1], Abdolrahim Taheri [2]

[1]*MSc Student, Petroleum University of Technology, Department of offshore structural engineering; Iran; Rasoul.Sadian@put.ac.ir*
[2]*Assistant Professor, Petroleum University of Technology, Department of offshore structural engineering; Iran; rahim.taheri@put.ac.ir*

ARTICLE INFO

Article History:
Received: 26 Apr. 2016
Accepted: 15 Jun. 2016

Keywords:
Existing Fixed Platforms, In-place Analysis, Pile-Soil Interactions, Persian Gulf

ABSTRACT

Offshore jacket structures have been used in petroleum industry for decades. Due to increasing the age of operating platforms, structural damages will be generated by corrosion, fatigue, ship impacts and other reasons. Improvements in the oil and gas recovery from several fields have raised the interest for using these platforms well beyond their intended design life. Life extension of an existing jacket platform needs proper reassessment of its structural members, such as piled foundations. This paper represents a case study of the existing fixed offshore platform located in Persian Gulf by in-place strength analysis. The objectives of this analysis are to verify whether the platform can meet the structural requirements, as per API RP 2A and AISC, for the In-place extreme met-ocean loading. The structural assessment is performed based on the best estimates of the existing conditions of the structure data on the future corrosion allowance. Since the response of the jacket platform to the environmental loads is intensely affected by the pile soil interaction, in current study the foundation is modelled using uncoupled non-linear soil springs acting along the piles length. The load cases, which include all situations relevant in the In-place analyses are taken into account. Results of the In-place analysis of the drilling platform indicate that the jacket structure does not assure the code provisions.

1. Introduction

Offshore jacket structures have been used in petroleum industry for decades. Due to increasing the age of operating platforms, structural damages will be generated by corrosion, fatigue, ship impacts and other reasons. Improvements in the oil and gas recovery from several fields have raised the interest for using these platforms well beyond their intended design life. Extension of the life of an existing jacket platform needs satisfactory reassessment of its different structural members, such as piled foundations. The existing platforms in the Persian Gulf area have typically been designed for a design life of around 25 years. The age distribution of the jacket platforms of this area shows that a relatively large number of installations are been passed the 25 years. The outcome of reassessment determines the subsequent course of action. For example, if a pile is reassessed and found to be "unsafe", structural intervention may be necessary or a new platform may be required. Both scenarios are very costly and this may eventually compromise the economic viability of a development. A rational reassessment of piles of existing platforms is therefore necessary to avoid costly solutions while ensuring that the underlying risk is as low as practically acceptable.

The process for assessment of existing platforms was proposed by Hugh Banon et all at 1994 [1]. Wisch et al [2] provided further background, clarification and proposal to update section 17 API RP-2A. API Recommended Practice 2SIM introduced to provide guidance to owner/operators and engineers in the implementation and delivery of a process to manage the structural integrity of existing fixed offshore platforms [3]. Reliability Based Assessment of Existing Fixed Offshore Platforms Located in the Persian Gulf was carried out by Alireza Fayazi and Aliakbar Aghakouchak [4]. A review of recent developments relating to structural reliability assessment of fixed offshore platforms can be found in [5] and [6]. This paper represents a case study for the structural evaluation of an existing platform

located in the Persian Gulf. The platform is now 47 years old and the objective of the study is to verify whether the platform can meet the structural requirements, as per API RP 2A and AISC. To check if it is fit for purpose for a life extension of 20 years beyond 2016. To provide a more exact and effective evaluation of offshore pile foundation systems under axial functional loads and lateral environmental loads, a finite element model software (SACS) is employed to consider the pile soil interaction. It should be noted that the structural model is based on the best estimates of the existing conditions of the platform.

In-Place Analysis of Jacket

In-place assessment is the structural analysis to assess the structural behavior of the jacket to specify its response service life. In-place analysis of jacket is carried out to control the global completeness of the platform against too early failure. Among all analysis of jackets, in-place is the most critical one. In a linear structural analysis with respect to ultimate limit state design (ULS), the specific capacity is normally taken as first yield or first component buckling [7]. If tubular members of a structure do not satisfy the ultimate strength provisions, resulting in yielding or buckling, the tubular member would not be considered fit for the purpose.

Analysis Software

SACS (Structural Analysis Computer Systems), a Design and Analysis software for offshore structures and vessels, is used for the modeling and analysis of the jacket. SACS is a finite element program for linear and nonlinear static and dynamic analysis of frame structures. Its ability to dynamically iterate designs allows users to perform advanced analysis, comply with offshore design criteria, and visualize complex results. SACS provides reliable beam member code checking and tubular joint code checking capacity; therefore, it is very suitable for topsides structures consisting of plate girders and tubular columns/ braces [8].

Structural Modeling

Platform Data

The jacket platform is eight-legged drilling jacket with grouted steel piles for the purpose of supporting 3415 tones maximum operation weight located in the Reshadat oilfield which is approximately located 108 km south west of Lavan Island in a water depth of around 58.8 m. The total height of the jacket is 87.4 m and the jacket footprint at sea floor is 30m×56m and leg spacing at working point is 41.15 m x 13.72 m. A perspective plot of the model is shown in Figure 1.

Three main components of the model are:
A) Substructure:

1. Jacket:
   a) Jacket legs
   b) Horizontal framings
   c) Elevation bracings and diagonals
2. Appurtenances

The following appurtenances are explicitly modelled for the hydrodynamic actions.

a) Fifteen conductors 22'' O.D (55.88cm)
b) One riser 18'' O.D (45.72cm)
c) One riser 6" O.D (15.24cm)
d) Two fire water pump caisson 18" O.D (45.72cm)
e) One fire water pump caisson 26" O.D (66.04cm)
f) Two J-tubes 8" O.D (20.32cm)

B) Foundation:

The foundation is modelled using uncoupled non-linear soil springs acting along the piles length. The load-displacement characteristics of these springs are defined by p-y, q-z and t-z curves based on geotechnical report. Based on pile makeup drawing the pile is modelled to a penetration of 41m below mud-line for all piles. Pile outer diameter is 762 mm. The scour readings by survey report ranged from 400mm to 900mm, so the final scour for modelling the platform was assumed equal to 1m on all pile locations.

C) Deck:

The topside has three deck levels and includes accommodations and different equipment. The model includes all the deck primary and secondary beams, truss chords, bracing and columns. Deck plates have been included as quadrilateral isotropic plate element for the in-plane stiffness of the deck.

Material

As per API RP 2SIM 2014 material specifications and properties of an existing structure are defined based on data from original design.

Table 1: Material properties [9]

Density		ρ=7850 kg/m3
Young's modulus		E=2.1·1011 Pa
Poisson's ratio		ν=0.3
yield strength (MPa)	$t \leq 16$	235
	$16 < t \leq 40$	225

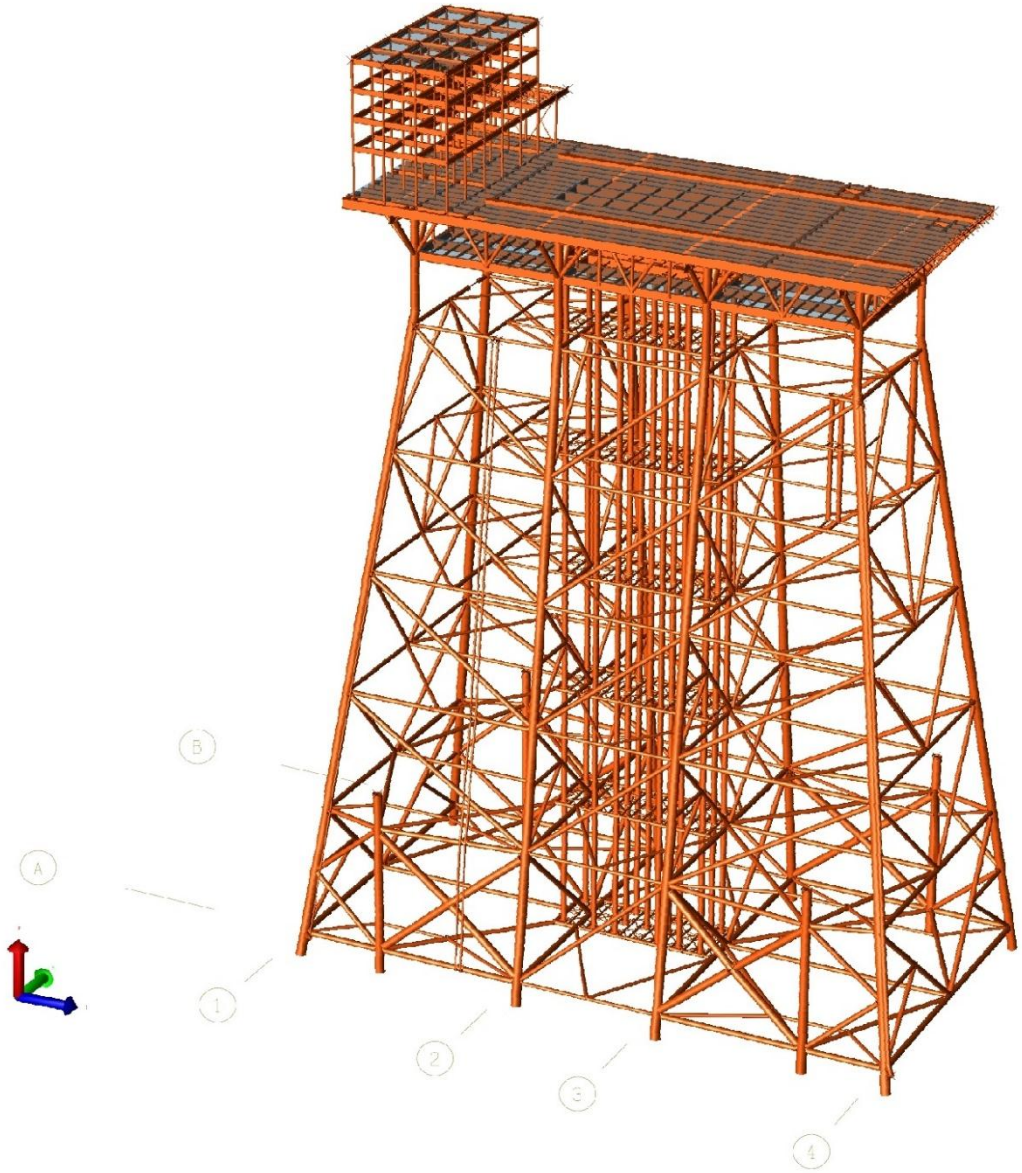

Figure 1: A perspective plot of the SACS model

Environmental Data

Water Depth

The platform is located in 193 feet (58.83 m) water depth. The design water levels and tidal range with 100 years return periods are summarized in Table 2.

Table 2: Water depth and surface fluctuations (m)

Description	One Year	100
Chart Datum Water Depth (To LAT)	58.8	58.8
Mean Sea Level (MSL)	1	1
MHHW	1.6	1.6
HAT	2	2
Storm Surge	0.2	0.3
Possible Subsidence*	+0.5	+0.5
Uncertainty Allowance	±0.5	±0.5
Maximum Water Depth	61.5	61.6
Minimum Water Depth	58.8	58.8

The maximum water depth considered in the analysis is 61.6m and the minimum water depth is 58.8m.
Max. Water Depth = Water Depth + HAT + Storm Surge + Subsidence

Wind

The wind loads are calculated based on the API RP 2A, using following-directional wind speeds for extreme storm conditions.

Table 3: 100-year return period wind speed (m/s)

Directio	NW	W	SW	S	SE	E	NE	N
wind	28.	27.	25.	25.	27.	27.	26.	27.

Shape coefficients for perpendicular wind approach angles with respect to each projected area should be considered as follows (API RP2A-WSD-2014):

Beams	1.5
Sides of buildings	1.5

Cylindrical sections	0.5
Overall projected area of platform	1.0

Wave and Current

Directional waves are used for the in-place analysis. Wave height with associated period for extreme storm conditions are as follows:

Table 4: 100-years wave heights and associated wave periods

Direction from TN	Maximum Wave Height, Hmax (m)	Significant Wave Height, Hs (m)	Wave Period, (sec)
NW	12.2	6.6	11
W	10.8	5.8	10.4
SW	8.8	4.7	9.5
S	10.2	5.5	10.2
SE	11.6	6.2	10.8
E	10.8	5.8	10.4
NE	8.8	4.8	9.6
N	9.7	5.2	10

The following currents are considered for the design of the platform.

Table 5: 100-years return period current profile (m/s)

Elevation	NW	W	SW	S	SE	E	NE	N
Surface	1.1	0.9	0.8	0.9	1.1	0.9	0.9	0.9
50% Water	0.8	0.6	0.5	0.6	0.8	0.6	0.6	0.6
5.0m above	0.5	0.4	0.3	0.4	0.5	0.4	0.3	0.4
0.5m above	0.4	0.3	0.3	0.3	0.4	0.3	0.3	0.3

Hydrodynamic Coefficients

Basic drag and inertia coefficients used to evaluate wave forces on cylindrical members are as follows:

Table 6: Hydrodynamic coefficients for calculating the storm wave loads on tubular members

Surface Conditions	Cm	Cd
Clean Steel	1.6	0.65
Marine Growth Fouled	1.2	1.1

For the In-place condition modelling, the wave kinematics factor should be taken as 0.9 as per API RP-2A. The current blockage factors for the 8 legged structures are as API RP-2A.

- End-on 0.70
- Diagonal 0.85
- Broadside 0.80

Marine Growth Profile

Marine growth may give rise to increased weight, increased hydrodynamic added mass and increased hydrodynamic actions, and may influence hydrodynamic instability. For typical design situations, global hydrodynamic action on a structure can be calculated using Morison's equation, with the values of the hydrodynamic coefficients for unshielded circular cylinders [10]. Table 7 presents the marine growth thickness measured by underwater survey. The specific weight of marine growth in air considered equal to 14 kN/m3.

Table 7: Marine growth thickness [3]

Top elevation (m)	Bottom elevation (m)	Thickness (mm)
0.00	0.3	5.0
0.3	14.9	5.0
14.9	15.5	5.0
15.5	27.1	5.5
27.1	27.7	4.0
27.7	39.3	4.0
39.3	39.9	6.0
39.9	51.5	6.0
51.5	52.1	6.0
52.1	63.7	6.0

Soil Condition

The analysis includes the effect of the non-linear soil stiffness through the soil-structure interaction software named SACS PSI. The soil model is subdivided into seven layers. The design soil parameters are presented in Table 8.

Table 8: Parameter values for R4 platform existing pile capacity

Layer number	Depth (m)	Soil type	δ (deg)	Cu top	Cu bot.	Sub. unit wt. (kN/m3)	Nq	f_{lim} (kPa)	q_{lim} (MPa)
1	0-16	clay	-	5	50	8	-	-	-
2	16-17.8	calcarenite	20	-	-	9	12	15	3
3	17.8-32	clay	-	55	85	8	-	-	-
4	32-49	calcarenite	23	-	-	9	15.8	15	5
5	49-60	clay	-	110	180	9	-	-	-
6	60-71.3	calcarenite	20	-	-	9	12	15	3
7	71.3-100.3	clay	-	150	220	9	-	-	-

Where:

δ = soil-pile friction angle
Cu = undrained shear strength
Nq = bearing capacity factor
f_{lim} = limit unit skin friction (kPa)
q_{lim} = limit unit end bearing pressure (MPa)

Methodology

The jacket components such as legs, primary and secondary braces and joints are designed to satisfy the strength and stability requirements specified in API RP2A-WSD and AISC-WSD. The check is performed through the use of the equations presented in these standards that can deliver the usage factor. If the usage factor is greater than 1.0 then the member is overloaded and does not meet the criteria for fitness for service. In-place analysis comprises three-dimensional static analysis with Pile Structure Interaction (PSI). As per API RP 2A the 100 years met-ocean storm data should be used for Design Level assessment [3].

Hydrodynamic Modelling

Jacket members in the splash zone are modelled with corrosion allowance (3mm during 20 years from now on [11]). The following consideration and parameters have been used in generating the water particle velocity and accelerations for wave loading in accordance with Morrison equation:

1. In-place analysis is carried out for minimum and maximum water depth cases.
2. Wave, current and wind loads are assumed to be collinear.
3. Stokes wave theory has been used for the wave load generation.
4. Seventy-two (72) wave positions of 5° intervals (full cycle) were stepped through the structure to identify the wave crest position causing the maximum base shear or the maximum overturning moment. The crest positions associated with the maximum base shear and the maximum overturning moment have been selected for the orthogonal and diagonal waves respectively.
5. A wave kinematic factor of 0.90, for extreme storm waves (API RP 2A-2014-5.3.1.2.4) has been considered.
6. Current blockage factors 0.80 (broadside), 0.7 (end-on) and 0.85 (diagonal) has been considered (API RP 2A-2014-5.3.1.2.5).
7. An apparent wave period, accounting for the Doppler effect of the current on the waves, has been determined (API RP 2A-2014-5.3.1.2.2).
8. A nonlinear stretching approach has been employed to stretch the current profile to the local wave surface.

Results and Discussion

Linear static analysis is performed for the eight legged jacket in 8 loading directions, 4 in orthogonal direction and 4 in diagonal directions. Post, a sub program of SACS VI, is used to calculate element stresses and compare them to allowable stresses. The API RP2A-WSD [12] and AISC-WSD [13] code are selected to check stresses in the elements. The check is performed through the use of the equations presented in these standards that can deliver the usage factor. If the usage factor is greater than 1.0 then the member is overloaded and does not meet the criteria for fitness for service. The basic allowable stresses are increased by 1/3 for the storm load cases.

Member Unity Check

A member check of a frame's structural member is performed to assess whether the member is subjected to acceptable stress levels. Calculation results show that under 100-year storm load condition, a total number of 44 members have had stress utilization factors (UCs) greater than unity. 24 members are located in the splash zone of the platform. They are believed to suffer from serious corrosion. Five critical members are secondary beams in main deck that are affected by local loading of equipment. These members have poor section (channel and angle sections) which seems have not sufficient section for local loadings and need to be reinforced or stiffened. Figure 2 presents the graphical summary on the whereabouts of code-noncompliance members identified in the course of the assessment analysis in existing condition.

Joint Unity Check

A punching shear check is carried out on the brace member at a joint to assess the shear through the chord. As for the other checks, these assessments are made through the use of a punching shear interaction equation that delivers a usage factor. A total number of 52 joints have had utilization factors (UCs) greater than unity. A lot of these joints are located in splash zone.

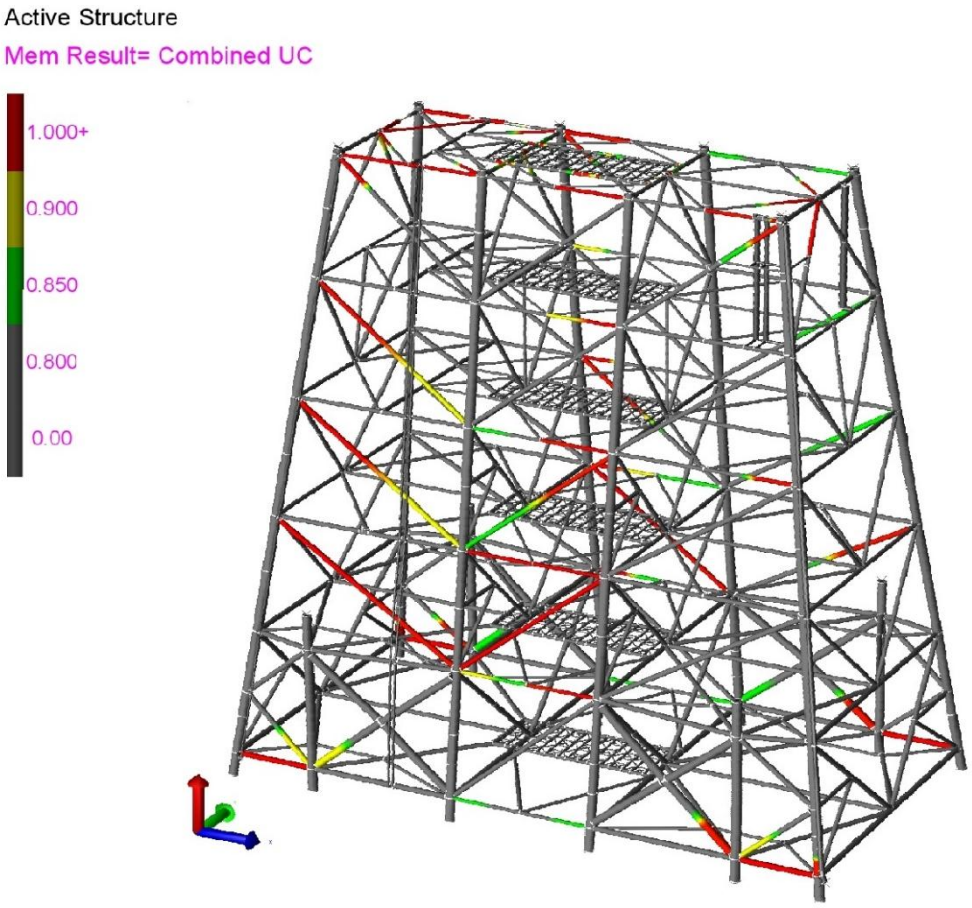

Figure 2: 3D Model for Jacket Members with UC >1.0

Piles Structural Strength (below Mud-line)

Piles do not meet the In-place structural code provisions as all piles have stress utilization ratios above unity. It should also be noted that no soil aging effect (the increase of soil shear strength with time) has been considered in obtaining the pile load bearing capacity.

Table 9: Pile below mud-line structural UC

Grid Location	Pile Joint No.	Pile below Mud-line Maximum Structural UC
A1	101L	1.11
A2	107L	1.10
A3	113L	1.10
A4	119L	1.16
B1	181L	1.22
B2	187L	1.18
B3	193L	1.18
B4	199L	1.21
Skirt Piles	J111L	1.25
	J113L	1.24
	J171L	1.32
	J173L	1. 36

Pile-head Displacement

The displacements of the platform in existing condition are not in allowable range. It seems this is because of unacceptable performance of the piles. The allowable lateral displacement at the pile-head is taken to be 10% of the pile diameter (7.6 cm =0.1D) as stated by ASTM STP-835 (1983) [14]. A similar ratio has been considered for the allowable axial displacement at the pile-head.

Table 10: Maximum pile-head displacements

Grid Location	Pile Joint No.	Displacements	Pile-head Displacement (cm)
A1	101L	Axial Dis.	38.87
		Lateral Dis.	14.95
A2	107L	Axial Dis.	38.25
		Lateral Dis.	13.68
A3	113L	Axial Dis.	35.55
		Lateral Dis.	13.94
A4	119L	Axial Dis.	32.17
		Lateral Dis.	14.91
B1	181L	Axial Dis.	41.95
		Lateral Dis.	12.22
B2	187L	Axial Dis.	44.9
		Lateral Dis.	12.55
B3	193L	Axial Dis.	45.88
		Lateral Dis.	12.55
B4	199L	Axial Dis.	46.55
		Lateral Dis.	11.95

Skirt Piles	J111	Axial Dis.	35.87
		Lateral Dis.	13.36
	J113	Axial Dis.	32.00
		Lateral Dis.	14.16
	J171	Axial Dis.	41.51
		Lateral Dis.	13.67
	J173	Axial Dis.	44.28
		Lateral Dis.	14.45

Topside Displacement

Topside displacements for different nodes at the main deck elevation and helideck elevation were obtained from the analysis. The H/200 limit for the deck deflection under the 100 year is based on AISC-2005 Commentary on Specification for Structural Steel Building-L4 Drift [13].

Table 11: maximum Topside displacements for different scenarios

Location	Maximum Overall Horizontal Displacement	Pile-head Lateral Displacement	Maximum Drift Relative to the Pile-head	Height Above Mud-line (m)	Allowable Drift
Main Deck	103.22	14.95	88.27	74.37	37.18
Helideck	140.95		126	87.62	43.81

Summary and conclusions

The structural integrity of the existing platform has been carried out as per In-place assessment provisions of API-RP-2A. The structural assessment was performed based on the best estimates of the existing conditions of the structure data on future corrosion allowance (3mm during 20 years from now on). The summary of the analysis result for the existing condition of platform are as below:

- Results from the analysis show that the existing platform does not assure the code provisions. This is mostly due to the poor performance of the piles, in addition to some members and tubular joints which experience utilizations factors greater than unity.
- Piles does not meet the code provisions as all piles have stress utilization ratios above unity. It should also be noted that no soil aging effect (the increase of soil shear strength with time) has been considered in obtaining the pile load bearing capacity.
- Calculation results show that under 100-year storm load condition, a total number of 44 members have had stress utilization factors (UCs) greater than unity. Of these, 24 members are located in the splash zone of the platform. They are believed to suffer from serious corrosion. Five critical members are secondary beams in main deck.
- In addition, a total number of 52 joints have had utilization factors (UCs) greater than unity. A lot of these joints are located in horizontal plans.
- The displacement of the platform in existing condition are not in allowable range. It seems this is because of unacceptable performance of the piles.
- Results of the In-place analysis of the drilling platform indicate that the jacket structure does not assure the code provisions. Therefore, it is mandatory to verify that the structures can fulfill the requirements of the nonlinear analysis. So, a nonlinear quasi-static (push-over) analysis is suggested for the further research about this specific platform.

References

[1] J. R. Krieger, W. F. and Lloyd, "Process for Assessment of Existing Platforms To Determine Their Fitness for Purpose," *Offshore Technol. Conf.*, pp. 131–140, 1994.

[2] L. Wisch, D. J., Puskar, F. J., "An Update on API RP 2A Section 17 for the Assessment of Existing Platform," *Offshore Technol. Conf.*, 2004.

[3] API, *Structural Integrity Management of Fixed Offshore Structures*, no. March. 2013.

[4] A. Fayazi, Alireza and Aghakouchak, "Reliability Based Assessment of Existing Fixed Offshore Platforms Located in the Persian Gulf," *Int. J. Marit. Technol.*, vol. 4, 2015.

[5] T. Moan, "Development Relating to Platform Requalification," 2015.

[6] V. J. Onoufriou, T., and Forbes, "Developments in Structural system reliability assessments of fixed steel offshore platforms," *Reliab. Eng. Syst. Saf.*, vol. 71, pp. 189–199, 2001.

[7] R. Faseela, A and Jayalekshmi, "In-Place Strength Evaluation of Jacket Platforms and Optimization of Bracing Configurations," *Int. J. Res. Advent Technol.*, no. June, pp. 10–11, 2015.

[8] SACS Suite program, *version 5.3*. 2011.

[9] DIN, "German Institute for Standardization."

[10] ISO 19902, "Petroleum and natural gas industries — Fixed steel offshore structures," 2007.

[11] Gerwick, "Construction of Marine and Offshore Structures," 2007.

[12] American Petroleum Institute, "Recommended Practice for Planning, Designing and Constructing Fixed Offshore Platforms - Working Stress Design," vol. 22nd Editi, 2014.

[13] American Institute of Steel Construction, "Steel Construction Manual," vol. 14th Editi,

2011.

[14] ASTM STP 835, "Laterally Loaded Deep Foundation: Analysis and Performance Panel Discussion at the ASTM Symposium on Laterally Loaded Deep Foundation," 1983.

INTERNATIONAL JOURNAL OF
COASTAL & OFFSHORE ENGINEERING IJCOE Vol.1/No. 3/Spring 2016 (43-50)

Available online at: http://ijcoe.org/browse.php?a_code=A-10-96-1&sid=1&slc_lang=en

The Effects of Internal Waves on Speed of Sound near Strait of Hormuz

Mojtaba Zoljoodi[1*], Afshin Mohseni Arasteh[2], Mojgan Ghazi Mirsaeid[3]

[1] Corresponding author: Faculty member and assistant professor, Iranian National Institute for Oceanography and Atmospheric sciences (INIOAS), email: zoljoodi@inio.ac.ir*
[2]Associated professor of Azad University, faculty of marine science and technology, North branch
[3]National Institute of Oceanography and Atmospheric Science

ARTICLE INFO

Article History:
Received: 30 Aug. 2017
Accepted: 20 Dec. 2017

Keywords:
Internal Wave
Sound Propagation
Vertical and Horizontal Movements

ABSTRACT

The internal waves complicate the propagation process of sound in the water. These waves are considered the main cause of disturbances in sound speed, and now it is known that the internal waves are the dominant parameter in the change process of sea frequency spectrum, as these changes range from many hourly cycles (floating frequency) to almost one daily cycle (inertia frequency).

The profile of mass sound speed in shallow waters depends on salinity and temperature gradients in turbulence internal waves. Here, the assumption is that the only probability function source is the turbulence internal waves in a water column. This investigation aims to use the mathematical models to study the internal wave effects on propagation of sound waves in shallow waters and that the waves how affect the sound propagation and depend on what parameters? We used the data gathered from Persian Gulf to calculate the parameters such as: sound speed, floating frequency, the ratio of resulted turbulences in sound propagation by vertical movement, phase functions and internal wave domain. Meantime, based on a given wave length (in the study area: 235 m.), the shape of first mode has been compared to the other modes. The probability density functions have been calculated for two different modes.

Comparing the ratio of generated turbulences in sound propagation by vertical movement and horizontal speed of particle, showed the horizontal movement is considerably less than the vertical one and also by increasing the depth (consequently decreasing the floating frequency), vertical movement is raised highly. The highest floating frequency and turbulences generated in sound propagation by vertical movement are found on the places near the water level and this is due to thermocline existence and on the other hand in the same places we have the lowest range of vertical movement.

1. Introduction

Marine environments mainly have the density stratification as they are in the forms of stepwise and continuous. While, the penetrative flow in the fluid with density stratification entered, the internal waves are generated and the penetrative flow energy propagates in vertical direction. Basically, the internal waves are existing in entire oceans but there is high probability of their existence in the gulfs and seas [1]. Sound waves regarding the energy transmission inside of the water is relatively stronger than the electromagnetism kinds [2]. So respect to the importance of both these waves in seas, this research investigates their effects in shallow waters.

2. The impact of internal wave turbulence on sound speed in shallow waters:

In shallow waters, the mean density is increasing by water depth linearly, so we have this function:

$$\bar{\rho}(z) = \rho_s + bz \quad (1)$$

where ρ_s is the water level density and b is the density gradient. Using the above relation and hydrostatic pressure formula, the pressure function in turbulence state is written as follows:

$$\bar{p}(z) = p_s + g(\rho_s + 1/2bz^2) \quad (2)$$

Where ρ_s is the atmosphere pressure, and g is magnetic velocity. But for shallow water, the above relation could be written as:

$$\bar{p}(z) = p_s + g\,\rho_s z \tag{3}$$

A function is presented by Ecart for the temperature as below:

$$\bar{T} = (2A)^{-1}[-B-(B^2-4AC)] \tag{4}$$

$$\begin{aligned} A &= -0.375 + 0.33625\bar{\rho} \\ B &= 38 - 37.424\bar{\rho} \\ C &= \bar{p}(1-0.698\bar{\rho}) + 5995 - 5831.01\bar{\rho} \end{aligned} \tag{5}$$

$\bar{T}$ in degree Celsius, $\bar{p}$ in atmosphere and $\bar{\rho}$ in gr/cm^3 are measured.

The speed of non-turbulent sound is calculated by below relation:

$$\begin{aligned} \bar{C}(z) = 0.3048[&4739.9 + 15\bar{T} - 0.1456\bar{T}^2 \\ &+0.01826 + 4.3(S-34)] \end{aligned} \tag{6}$$

And as we assumed the study area should be enough shallow the depth impact (z) could be ignored, as the below relation:

$$\bar{C}(z) = 0.3048[4739.9 + 15\bar{T} - 0.1456\bar{T}^2] \tag{7}$$

The mean sound speed profile could be calculated and plotted through the following provisions:

$\rho_s = 1.0223 gr/cm^3$, $p_s = 1at$, $H \approx 70m$.

The equation of vertical speed of internal wave with its boundary conditions, has been written as below:

$$\nabla^2 W_{zz} + N^2 \nabla_H^2 W + f^2 W_{zz} = 0 \tag{8}$$

$$W(x,y,0,t) = W(x,y,-D,t) = 0 \tag{9}$$

The above equation for a constant N^2, results as follows:

$$W = \varphi(z)\exp[i(kx + ly - \omega t)] \tag{10}$$

Where, $\varphi(z)$ is the range of vertical speed and ω is the internal wave frequency. $\varphi(z)$ Should be written as below in order to be applied in the relation of vertical speed of internal wave:

$$\varphi_n(z) = A_n \sin(n\pi z / D) \tag{11}$$

The index ***n*** shows the number of normal mode. The first mode has the high importance, as it includes usually the biggest range and shows low tension comparing to the high level modes. The internal wave frequency by wave length as: $L = 2\pi\left(k^2 + l^2\right)^{-1/2}$ could be changed to the below relation:

$$\omega_n = \left\{\left[4N^2 + (\frac{L}{H})^2 f^2 n^2\right]\left[4 + (\frac{L}{H})^2 n^2\right]^{-1}\right\}^{1/2} \tag{12}$$

The vertical speed while it is ***n=1*** by combining the relations (11) and (12), and separating its real section could be written as below:

$$W_1(x,y,z,t) = A_1 \sin(\frac{\pi z}{H})\cos(kx + ly - \omega_1 t) \tag{13}$$

The integration of relation (13) relative to the time results in the vertical movement as follows:

$$\gamma(x,y,z,t) = \Gamma \sin(z\pi / H)\sin(kx + ly - \omega_1 t) \tag{14}$$

Where, $\Gamma = -A_1/\omega_1$ has been considered the movement range. Thus for each following variables: *t*, *y*, *x*, the γ constant varies in the water column as sinusoidal.

The equations (4), (5) and (7), result in changes of temperature and sound speed profile. The variation of sound final speed is almost equal with the vertical movement of water multiplied by $\left(d\bar{C}/dz\right)$, so we have:

$$C_1(x,y,z,t) = \Gamma \frac{d\bar{C}}{dz}\sin(\frac{\pi z}{H})\sin(kx + ly - \omega_1 t) \tag{15}$$

And, the total speed of sound is written as:

$$\begin{aligned} C(x,y,z,t) &= \bar{C}(z) + \\ &\Gamma \frac{d\bar{C}}{dz}\sin(\frac{\pi z}{H})\sin(kx + ly - \omega_1 t) \end{aligned} \tag{16}$$

The above relation indicates the standard deviation of internal wave speed.

3. The interaction of sound wave accelerator and internal Solitons:

Orr and Baxter [3] based on ray theory worked on this issue and they studied the effect of ocean internal wave on short-range sound propagation and full frequency. The results revealed that the reaction of sound propagation frequency in shallow waters and summer time mostly depends on time and propagation direction and occasionally it illustrates a high weakness in some frequency domains. These waves exist in shallow waters as non-probability groups with given wave lengths and defined as alone waves or Solitons [4]. The transition of energy happens usually between the modes with special difference of its values could be equal to wave peak of internal wave spectrum or roughness of bed floor, it means:

$$k_{\text{int}} = \frac{2\pi}{\lambda_i} = k_n - k_m \tag{17}$$

Where, k_{int} is almost equal to special difference of values among normal acoustic modes. As an example:

$$\lambda_i = 235 \rightarrow k_{\text{int}} = \frac{2\pi}{235} = 0.026736 \qquad (18)$$

The equation below clearly indicates that why considerable amount of energy is transferred by the first mode to the high level modes and so why and where the frequency intensifying of acoustic wave and wave length of Solitons happen [Figure 1].

$$k_L L_p = \left(n + \frac{1}{2}\right)\pi \qquad (19)$$

L_p is the internal wave length [5].

Regarding to each special wave length (in the study area λ=235m.), the shape of first mode is quite different than the other modes, but about else wave lengths, the shapes are too close to the first mode. As a lot of energy is transferred from the first mode to the high level modes, in the longer waves the coupling effect of mode is considerably weak [6].

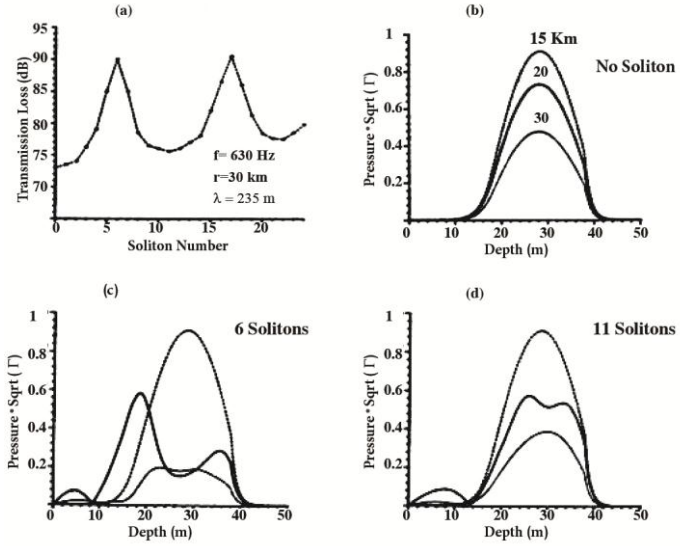

Figure 1. Intensifying of soliton wave length (a). Depth distribution function for various wave lengths (b-c-d) Zhou, Ji-Xun., 1991[۱].

4. Interaction of internal wave and acoustic in long-range

We assume internal wave movement could be written as below:

$$\eta(r,z,t) = \eta_D(r,z,t) + \eta_S(r,z,t) \qquad (20)$$

Where, η_D indicates the diffusion component and η_S is the Soliton portion [7].

At the moment, internal waves diffusion component in shallow waters is considered an important research topic. Diffusion field component is considered as a statistical combination from horizontal waves that is covered by Garret-Munk spectrum.

This issue uses a special orthogonal set of internal wave functions to expand $\eta_D(r,z,t)$, as it is obtained from linear equation of Navier-Stokes for stratified inviscid and sparse fluid. In this condition the diffusion field is defined as a weighted two fold summation on ***J*** number and horizontal wave number $(k_h = (k_x^2 + k_y^2)^{\frac{1}{2}})$:

$$\eta_D(r,z,t) = \sum_{k_h}\sum_{j} F(k_h, j) W(k_h, j, z) e^{i[k_h r - \omega(k_h, j)t} \qquad (21)$$

In the relation above the average of weight factors are equal to zero.

Using k_h we assume that the internal wave field is homogenous horizontally. While, shear flow is considered negligible in the water column the diffusion relation $w(k_h, j)$ and special functions related to depth $W(k_h, j, z)$ in special equation of amount is applied as below:

$$\frac{d^2}{dz^2} W(z) + k_h^2 \left[\frac{N^2(z) - \omega^2}{\omega^2 - f_c^2}\right] W(z) = 0 \qquad (22)$$

Where, ***N*** is the floating frequency or Brunt-Vaisala frequency [8].

$$N^2(r,z) = -\frac{g}{\rho}\frac{\partial}{\partial z}\rho_p(r,z) = g\left(h\frac{\partial T_P}{\partial z} - s\frac{\partial s}{\partial z}\right) \qquad (23)$$

For the condition of rigid boundary we have as:
W(0)=W(H)=0.

Where, ***H*** is the water depth and the Coriolis frequency is obtained from the following relation: $f = 2\Omega\sin$ [illegible] . Ω is the angle speed of earth. The results of equation (22) are independent from any range and so we ignore the coupling of internal wave mode that depends on the relation`s range with floating frequency. Now, by the result of partial equation range for coupling of acoustic mode, we are allowed to insert the dependence of range into the equation (21), whiles this dependency is applied for the bed by boundary condition. To simplification in the calculation of η_D the parameter of time has been taken into account equal to zero. This option revealed that the average values of acoustic field have been calculated by the samples which provide time intervals longer than the time to complete internal waves field (about many minutes).

As an instance; the floating frequency and sound speed profile have been calculated using the data sets of a device installed in the Persian Gulf at 2001 (Figure 2).

This profile illustrates the structure of a layer quasi waterway in a depth of 20m. by salinity and temperature gradient in a water column [9].

Special amount $w(k_h, j)$ and special functions $W(k_h, j, z)$ are calculated by equation (22) in a domain $k_h\{0.0002, 0.25\}m^{-1}$ which is correspondent to horizontal wave length from 25 to 31/4 km. Such range of wave covers spatial scales which are important for acoustic calculations in this investigation. The depth of water has been taken into account about H=70m. and the latitude of 30º N is chosen for coriolis frequency measurement.

The exponential spectrum that is related to $F(k_h, j)$ has been assumed as Garrett-Munk spectrum [10]:

$$<|F(k_h, j)|^2> = E_0 M [j^2 + j_*^2]^{\frac{-p}{2}} (\frac{4}{\pi}) k_j k_h^2 (k_h^2 + k_j^2)^{-2} \quad (24)$$

The quantity of k_j is obtained by $k_j = (\pi i f_c) / \int_0^H N(z) dz$ and for j[th] mode with the spectrum peak is related to dominant horizontal wave number. The normalize parameter of ***M*** defined by $\frac{1}{M} = \sum_{j=1}^{x} [j^2 + j_*^2]^{\frac{-p}{2}}$. The parameter of E_0 indicates the average of energy density (J/m^2) and it is in relation with the exponent of internal wave oscillation. The features of wave number as j_*, and exponent of spectrum as ***P*** experimentally define the parameters which control the relative modes of internal waves.

The amount of E_0 in most of simulations is J/m^2 ۲۵, it means that 10% of E_0^{max} has been chosen and it is physically rational. The weight factor of mode (p) is considered [8].

An example of sound speed fluctuations δc that is in relation to the field of diffusion internal wave η_D has been shown in figure 3 with the sound speed component. These fluctuations depend on both depth and range. The variations of depth and range averages are calculated by mean sound speed $<(\delta c / c)^2> \approx 0.5(10^{-6})$. The fluctuations are restricted to an area of thermocline where maximum share of temperature and salinity are floating on frequency whiles the high level modes have relatively smaller shares on the total spectrum and in understanding of acoustic diffusion are considered so important, as vertical structure of high level modes generate much more acoustic diffusion comparing to the low level modes as well as the modes without structure.

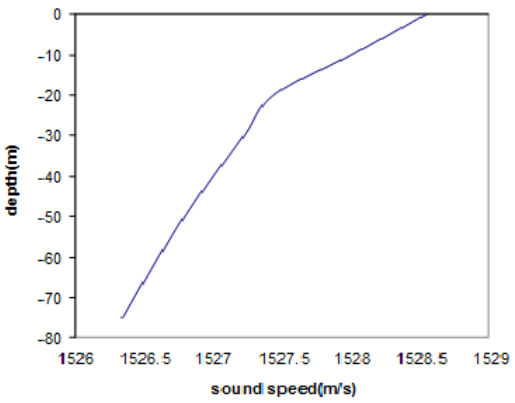

Figure 2. Calculation of sound speed profile using the data sets of a device installed near Hormuz Strait at 2001.

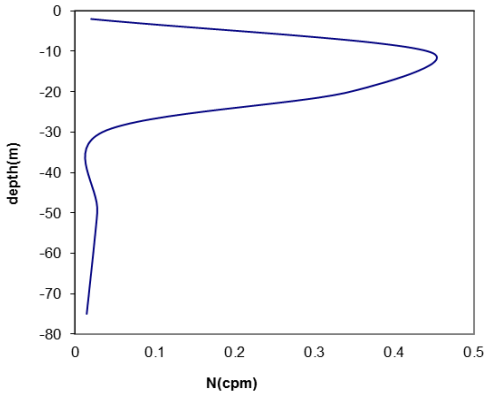

Figure 3. Calculation of buoyancy frequency using the data sets of a device installed in the Persian Gulf near Hormuz Strait at 2001.

In total, both domains of condition and phase influence the pressure field. On the other hand the calculations of deviation and mode velocities in the share of phase are negligible. Thus we have the relation as follows:

$$I_i(n, r, f) = d_i^* c(n, r, f) d_i(n, r, f) \quad (25)$$

The comparison of the obtained deviation coefficients indicates that the domain calculation only by considering 10 first modes includes many quality characteristics in entire field for the shortest ranges [Figure 4].

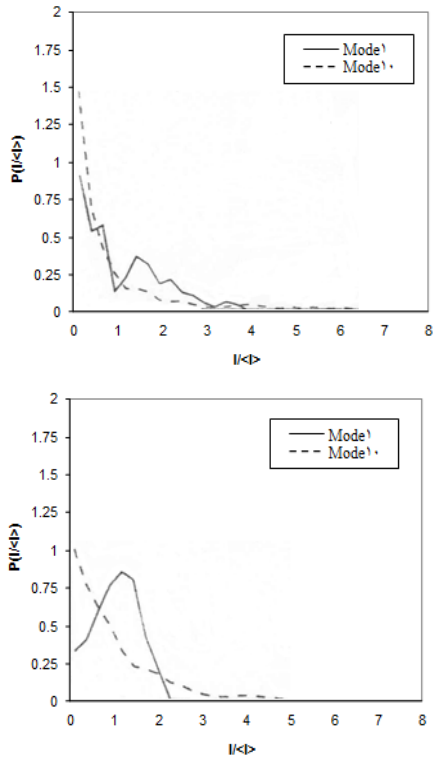

Figure 4. Probability density functions $Q(I_i(n,r,f)/<I_i(n,r,f)>)$ for the modes 1 and 10 (left) r=20km and (right) r=200km. in both cases density energy E0=100J/m^2 and the installation depth of assumed source is at 45m.

5. The mathematical model of internal wave effect on sound diffusion

The mathematical model is presented as below to consider the internal wave impacts on sound diffusion [11]. In this method the equation of acoustic wave pressure fluctuation is applied.

$$\nabla^2 P + \left(\omega_0^2/c^2\right)P = 0 \tag{26}$$

By writing $k = \omega_0/c_0$ and $\left(\omega_0/c\right)^2 = \omega_0^2/\left(c_0+\delta c\right)^2 \cong \left(\omega_0/c_0\right)^2\left(1+2\mu\right)$ and replacement of $P = p\exp\left(i\ 2\pi kx\right)$ in the equation (22) we will have:

$$\nabla^2 p + 2i2\pi k\partial_x p + 2\mu\left(2\pi k\right)^2 p = 0 \tag{27}$$

To define domain and phase of wave the relation below has been used:

$$p = e^{\psi} = Ae^{is} \quad ,i.e.\ .\ , \quad \psi = \ln A + iS \equiv \chi + iS \tag{28}$$

The above relation will change the equation (27) as below:

$$\nabla^2\psi + 2\ i\left(2\pi k\right)\partial_x\psi + 2\left(2\pi k\right)^2\mu = -\left(\nabla\psi\cdot\nabla\psi\right)^2 \tag{29}$$

Ignoring the non-linear phrases and through Fourier transform:

$$\mu(x,z,r) = \int d\beta\, d\omega\, v(x;\beta,\omega)\exp\left[2\ i\pi\left(\beta z - \omega t\right)\right] \tag{30}$$

$$\psi(x,z,t) = \int d\beta\ d\omega\ \bar{\psi}(x;\beta,\omega)\exp\left[2\ i\pi\left(\beta z - \omega t\right)\right] \tag{31}$$

So based on above relations, it is changed to a normal differential equation in terms of $\bar{\psi}$

$$\left[\partial_{xx}^2 + 2\ i\left(2\pi k\right)\partial_x - \left(2\pi\beta\right)^2\right]\bar{\psi} = -2(2\pi k)v \qquad \bar{\psi}\left(x=0;\beta,\omega\right) = 0 \tag{32}$$

The Fourier transform of phase (s) and domain (χ) is written as below:

$$\bar{s}\left(x;\beta,\omega\right) = \left(1/2i\right)\left[\bar{\psi}\left(\beta,\omega\right) - \bar{\psi}^*\left(-\beta,-\omega\right)\right], \tag{33-a}$$

$$\bar{\chi}\left(x;\beta,\omega\right) = \frac{1}{2}\left[\bar{\psi}\left(\beta,\omega\right) + \bar{\psi}^*\left(-\beta,-\omega\right)\right], \tag{33-b}$$

And as $\bar{v}^*\left(-\beta,-\omega\right) = \bar{v}\left(\beta,\omega\right)$, so we have:

$$\begin{Bmatrix}\bar{s}\\ \bar{\chi}\end{Bmatrix} = 2k\pi\int_0^x \bar{v}\left(x';\beta,\omega\right)\begin{matrix}\cos\\ \sin\end{matrix}\left[\frac{\pi\beta^2\left(x-x'\right)}{k}\right]dx' \tag{34}$$

$$<\mu^2> = \int_f^n d\omega\int_0^\infty d\beta\ \varphi_\mu\left(\omega,\beta\right) \tag{35}$$

And φ_μ is obtained by Garret-Munk model.

Thus, the index of diffraction spectrum will be resulted as follows [Figure 10]:

$$\Phi_\mu\left(\omega,\beta\right) = 2\times\left(\frac{2}{\pi}\right)^2\left\langle\mu^2\right\rangle f\,\frac{\left(\omega^2-f^2\right)}{\beta_*\omega^3}\,\frac{1}{\left[1+\left(\frac{\beta}{\beta_*}\right)^2\right]} \tag{36}$$

$$\begin{cases}\left\langle\mu^2\right\rangle = G\ n^2\left\langle\xi^2\right\rangle\\ \beta_* = t\left(n^2-\omega^2\right)^{\frac{1}{2}}\end{cases}$$

Also, similarly about φ_s we will have as [Figures 6 and 9]:

$$\begin{matrix}\varphi_S\left(\omega;\beta\right)\\ \varphi_\chi\left(\omega;\beta\right)\end{matrix} = 4\left(K/\beta\right)^4\varphi_\mu\left(\omega,\beta\right)\Im_\pm\left(\tilde{L},\Gamma\right) \equiv \mathrm{N}_\pm\varphi_\mu \tag{37}$$

Where:

$$\pm \equiv \int_0^{\tilde{L}} d\eta \; J_0(\Gamma\eta) \left[\left(\tilde{L}-\eta\right)\cos\eta \pm \cos\tilde{L}\sin\left(\tilde{L}-\eta\right)\right] \quad (38)$$

[Figures 7 and 8]

$$\tilde{L} = \pi\beta^2 L / k$$

$$\Gamma = \left(\frac{2k}{\beta}\right)\left[\left(\omega^2 - f^{\,2}\right)/\left(n^2-\omega^2\right)\right]^{\frac{1}{2}}$$

$$N_{\pm} \equiv 4\left(k/\beta\right)^4 \Im_{\pm} \quad (39)$$

$$\Im_{\pm} = \begin{cases} \left(\tilde{L} \pm \cos\tilde{L}\sin\tilde{L}\right)/\Gamma \\ 2\tilde{L}/\Gamma & \tilde{L} << 1 \\ 2\tilde{L}^3/(3\Gamma) & \\ \tilde{L}/\Gamma & \tilde{L} >> 1 \end{cases}$$

To calculate the max and min values of β, the Richardson Number is used . For simplifying of calculations, the frequencies relating to internal waves in *cph* and the acoustic signal frequencies in *Hz* are used.

Using their models, the produced disturbances by internal waves, domain spectrum and relative phase to vertical wave number, internal wave spectrum to vertical wave number and domain function and phase are calculated for a selected station in the Persian Gulf with geographic position of 27° 28`.50 N and 51°57`.01E , in 2001 marine cruise.

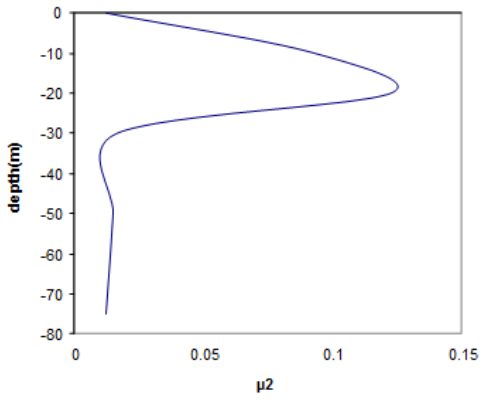

Figure 5. The produced disturbances by internal wave in vertical speed

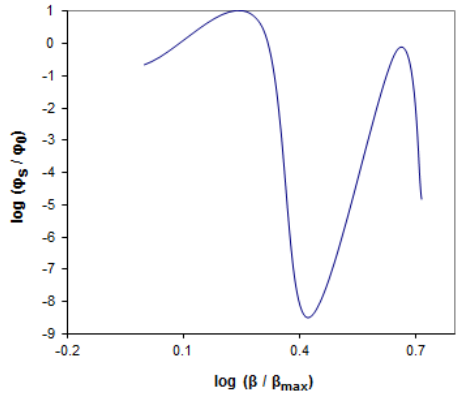

Figure 6. Phase spectrum into the vertical wave number

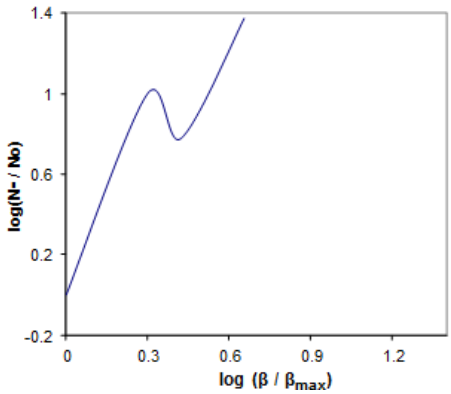

Figure 7. The function domain into vertical wave number

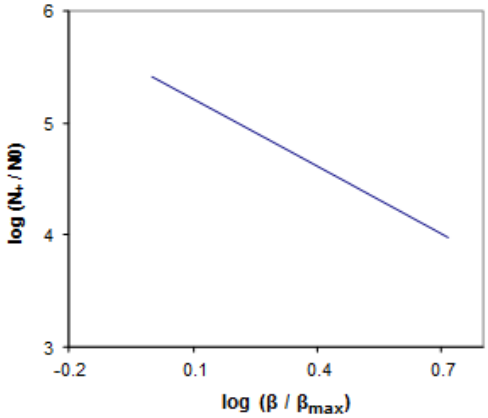

Figure 8. The phase function into vertical wave number

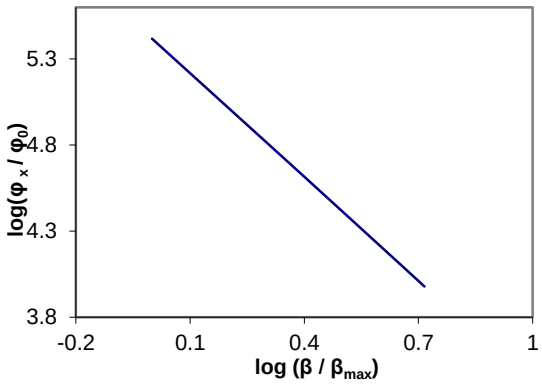

Figure 9. The domain spectrum into vertical wave number

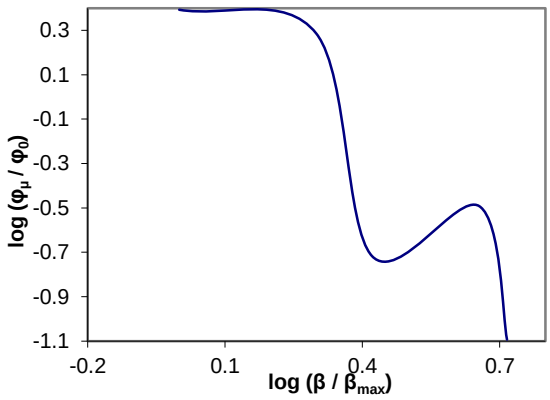

Figure 10. Internal wave spectrum into vertical wave number

Table 1. The sample of calculations for data derived from a sample station in the Persian Gulf near Strait of Hormuz , in 2001 marine cruise.

Depth(m)	μ^2	sound speed(m/s)	N(cpm)	log(N-/N0)	$\log(\beta/\beta_{max})$	$\log(\varphi_x/\varphi_0)$	$\log(\varphi_s/\varphi_0)$	$\log(\varphi\mu/\varphi 0)$	$\log(N_+/N_0)$
-10	9.29E-02	1528.005	0.4418472	-0.107634	0	5.4161	-0.657052	0.393397	5.4161
-20	1.23E-01	1527.438	0.3448281	0	0.2995	4.8164	0.612442	0.285728	4.8164
-30	1.64E-02	1527.225	0.0342646	1.0013114	0.4212	4.5721	-8.497586	-0.717028	4.5721
-50	1.49E-02	1526.792	0.0576210	0.7762278	0.6549	4.1009	-0.165614	-0.491293	4.1009
-75	1.22E-02	1526.340	0.0144245	1.3748308	0.7158	3.9773	-4.824745	-1.0927730	3.9773

6. Conclusion and discussions

- Regarding to the increase of energy density amount of the internal wave, the further fluctuation of sound speed and the regular stronger coupling mode are generated. In general, the attenuation amount of each especial mode depends on the coupled modes and also weakening coefficient of mode.
- Studying the different wave-lengths, shows that in a given wave-length the first mode shape is quite distinct than the other modes, whiles about the other wave lengths, the mode shapes are too similar to the first mode. Accordingly, the big amount of energy is transferred from the first mode to the high level modes, but in the higher boxes, the coupling effect of mode is very weak.
- Since, the acoustic phase of linear function is generated from internal wave movement, the domain fluctuation is resulted from intervention of many rays.
- If the share of internal wave field spectrum is by random, the domain and range also will be random. Understanding this question is important that the phase spectrum is proportionate with the internal wave spectrum, but the domain spectrum includes the frequentative components by the generated frequency change from internal wave. Thus when the domain and phase spectrums are random, so the phase information is belonging to the environmental parameters, whiles it is not so about the domain.
- The phase spectrum decreases with the internal wave frequency cubic and it is compatible with acoustic frequency range and root. The domain spectrum also similarly decreases with the internal wave frequency cubic. But it is independent from the acoustic frequency and range cubic. All these results are compatible with the theories. But relating to the phase it is also consistent with the available data.
- The biggest amount of floating frequency and the produced disturbances in the sound propagation because of vertical movement are shown on the area near to the water level and on the other hand in the same place the lowest vertical movement is happened, as the vertical movement increases as $n^{-1/2}$ with depth. Therefore, by the equation of $\mu = n^2(z)\zeta\sigma / g$, the fluctuation of sound speed by depth increases with the exponent 3/2 of floating frequency $\left(n^{3/2}\right)$.
- The biggest amount of floating frequency (N) is in the thermocline area and the lowest beside the bed, is available.
- Comparing the above graphics indicated that the internal wave floating frequency can affect the sound wave frequency. In first 20 meters of depth where the sound speed decrease rapidly, the floating frequency is maximum because of some formation principals of the water masses and density gradient, and consequently the highest disturbances in sound speed happed. The density gradient by depth increasing is weakening and consequently the floating frequency and generated disturbances in sound speed is minimized through the internal waves.
-

References

1- Zhou, Ji-Xun., (1991), *Resonant interaction of sound wave with internal solitons in the coastal zone*, J. Acoust. Soc. Am.90(4), 2042-2053.

2- Tielburger, D., Acou.Y. f., (1997), *Propagation through an internal wave field in a shallow water waveguide* , J. Acoust. Soc. Am.101(2), 789-807.

3- Orr, M. H., Baxter, L. and Hess, F. R., (1980), *Remote acoustic sensing of the particulate phase of industrial chemical wastes and sewage sludg*, Woods Hole Oceanogr.Inst., Woods Hole, mass., WHO1 Tech. Rep. 79-38, 153pp.

4- Desaubies, Y. f.,(1976), *Acoustic-phase fluctuation induced by internal waves in the ocean*, J. Acoust. Soc. Am.60(4), 795-800 .

5- S. M., 1975, " Effects of internal waves on sound pulse propagation in the straits of florida," J. Acoust. Soc. Am.58(6),1151-1158.

6- Bates, B. J., (1987), *Stochastic simulation and first-order multiple scatter solutions for acoustic propagation through oceanic internal waves*, J. Acoust. Soc. Am. 82 (6), 2042-2049.

7- Small, J. and Martin, J., (2002), *The generation of non-linear internal waves in the Gulf of Oman. Continental shelf research*, 22(8): 1153-1182.

8- Thorpe, S. A., (2005), *The turbulent ocean*, Cambridge University Press.pp 230.

9- Jackson, C., (2007), *Internal wave detection using the Moderate Resolution Imaging Spectroradiometer* (MODIS), J. Geophysical Research, VOL. 112, C11012.

10- Mohseni, A., Chegini v., Mirsaeid M., (2010), *A mathematical model of internal waves on sound (case*

study Caspian Sea), J. of Iranian marine science and technology, No.4, P.92-103.
11- Muacho, S., da Silva, J. C. B., Brotas, V. and Oliveira, P. B., (2013), *Effect of internal waves on near-surface chlorophyll concentration and primary production in the Nazaré Canyon (west of the Iberian Peninsula).* Deep Sea Research Part I: Oceanographic Research Papers 81(0): 89-96.